

¹ Hebb’s Vision: The Structural Underpinnings of Hebbian Assemblies

² J Wagner-Carena^{1,2,3}, S Kate^{*1,5}, T Riordan^{*1}, R Abbasi-Asl^{1,4}, J Aman¹, A Amster¹, AL
³ Bodor¹, D Brittain¹, JA Buchanan¹, MA Buice¹, DJ Bumbarger¹, F Collman¹, NM da
⁴ Costa¹, DJ Denman¹, SEJ de Vries¹, E Joyce¹, D Kapner¹, CW King¹, JD Larkin¹, J Lecoq¹,
⁵ G Mahalingam¹, D Millman¹, J Mölter⁶, C Morrison¹, RC Reid¹, CM Schneider-Mizell¹, S
⁶ Daniel¹, S Suckow¹, KT Takasaki¹, M Takeno¹, R Torres¹, D Vumbaco¹, J Waters¹, DG
⁷ Wyrick¹, W Yin¹, J Zhuang¹, S Mihalas^{†1}, and S Berteau^{†1}

⁸ ¹*Allen Institute, Seattle, WA, USA*

⁹ ²*Department of Molecular and Cellular Biology, Harvard University, Cambridge, MA, USA*

¹⁰ ³*Neuroscience Graduate Program, University of California, San Francisco, San Francisco, CA, USA*

¹¹ ⁴*Department of Neurology, University of California, San Francisco, San Francisco, CA, USA*

¹² ⁵*Department of Biomedical Engineering, Georgia Institute of Technology, Atlanta, GA, USA*

¹³ ⁶*Department of Mathematics, School of Computation, Information and Technology, Technical
University of Munich, Germany*

¹⁵ **1 Abstract**

¹⁶ In 1949, Donald Hebb proposed that groups of neurons that activate stereotypically
¹⁷ form the organizational building blocks of perception, cognition, and behavior.
¹⁸ He theorized that repeated activations induce the structural changes needed to group
¹⁹ neurons in these assemblies. Despite Hebb’s enduring influence, testing his predictions
²⁰ at relevant scales has been technically challenging. Here, we test the theory using a
²¹ novel, large-scale dataset featuring *in vivo* calcium fluorescence imaging of neural activity
²² with postmortem electron microscopy (EM) for detailed reconstruction of neurons
²³ from the same volume of mouse visual neocortex. A coregistration process matches
²⁴ EM-reconstructed neurons to their recorded fluorescence traces. From these traces, we
²⁵ extract neural assemblies from higher-order correlations in neural activity. We find
²⁶ multiple assemblies, many with overlapping neurons, and some neurons that do not
²⁷ participate in any assembly. We then show that these assemblies exhibit properties con-
²⁸ sistent with Hebb’s theory, including more reliable responses to repeated natural movie
²⁹ inputs than size-matched random ensembles and superior decoding of visual stimuli. Us-
³⁰ ing coregistration to probe structural correlates, we find that neurons that participate in
³¹ assemblies are significantly more integrated into the structural network than those that
³² do not. Contrary to Hebb’s original prediction, we do not observe a marked increase in
³³ the strength of monosynaptic excitatory connections between cells participating in the
³⁴ same assembly. However, we find significantly stronger indirect feed-forward inhibitory
³⁵ connections targeting cells in other assemblies. Intuitively, the delineation of assemblies
³⁶ can be realized either by internal excitation or external inhibition. Our findings support
³⁷ the latter mechanism. These results show the utility of assemblies in perception and
³⁸ provide a structural underpinning. They lay the foundation for future studies looking
³⁹ at the utility of assemblies in cognition and behavior, as well as the mechanisms for the
⁴⁰ formation and maintenance of such assemblies.

^{*}These individuals contributed equally to this work as second authors

[†]These individuals contributed equally to this work as senior authors

41 2 Introduction

42 Since Hebb's 1949 monograph, *The Organization of Behavior*[1], cell assemblies have
43 retained a persistent place in the imagination of the neuroscience community, both as
44 a prospective unit of functional organization and as a compellingly likely consequence
45 of simple rules of synaptic plasticity, such as the “fire-together wire-together” synapses
46 dubbed ‘Hebbian Synapses’ by Yves Frégnac in 1986 [2]. Throughout this work, we
47 follow Hebb in using the term assembly to refer to overlapping sets of neurons that acti-
48 vate in a reproducible pattern with high fidelity; in much of the contemporary literature,
49 such groups are also called cell ensembles or simply ensembles. The theory continues to
50 stimulate research on the activity-related aspects of assemblies, and the organization of
51 these processing modules is thought to operate through stable recurrent activity [3, 4].
52 Incorporating a behavioral approach, experimental evidence implies that the response
53 of discrete cell populations akin to assemblies may also have a causal link with motor
54 functions [5]. In particular, there has been confirmation of sequential activation within
55 neural assemblies of the primary visual cortex (V1) [6] as well as ongoing ‘replay’ of
56 coactivity in the absence of stimuli [7]. There has also been some limited evidence of
57 cell assemblies’ stability over long periods of time [8].

58 However, research examining the structural aspects of Hebbian cell assemblies has
59 primarily focused on the potentiation of synapses between excitatory neurons. This em-
60 phasis is perhaps not surprising, given that this potentiation has a place of prominence
61 in Hebb’s original formulation of the theory [1]. In 1963 [9], Hebb himself acknowledged
62 that his excitation-only formulation of assembly theory was a concession to the state
63 of research on inhibitory synapses at that point in time; synaptic inhibition of neural
64 activity was not confirmed until 1952 [10]. Over the following decades, the association
65 between Hebbian assemblies and excitatory potentiation has itself been reinforced by
66 the computational plausibility of excitatory plasticity as a mechanism of assembly for-
67 mation [11, 12, 13], and the discovery of Hebbian synapses. However, such changes were
68 never a necessary precondition for assembly formation. Mechanistically, there exists a
69 broad range of plausible solutions to assembly formation, ranging from excitatory mod-
70 ulation against a backdrop of relatively stable inhibitory strengths to the opposite, in
71 which formation relies solely on inhibitory modulation contrasting with stable excitatory
72 connections [14].

73 The approach of this work, using large-scale recordings of individual neurons to
74 identify and analyze assembly function, enters a developing tradition in the literature of
75 population dynamics [15, 16, 17, 18, 19, 20]. However, due to limitations in structural
76 analysis, few studies can relate the structure of assemblies to their function, as reviewed
77 by [14]. Electrophysiological datasets can allow highly reliable inference of connectiv-
78 ity in the case of multi-patch recordings, but with very small numbers of cells in any
79 given study. Extracellular recordings can overcome this limitation, but produce biased
80 connectivity estimates, and therefore cannot be considered a gold standard.

81 To relate the correlated activity of a large number of neurons to their connections, we
82 used a novel large-scale multi-modal dataset: the Allen Brain Observatory V1 Deep Dive
83 (V1DD) [21] (Fig. 1A). V1DD offers a combination of Ca^{2+} fluorescent recordings and
84 detailed EM reconstruction of neurons and synapses, including post-synaptic density
85 volumes. Taking advantage of advances in optical imaging techniques [22], V1DD pro-
86 vides multiple scans of high-quality simultaneous two-photon calcium imaging (2PCI)
87 recordings of thousands of excitatory neurons within the mouse primary visual cortex
88 (Fig. 1B). In addition to its functional recordings, V1DD also contains electron mi-
89 croscopy (EM) of the same tissue volume, which has uncovered the fine-scale anatomy
90 of the cubic millimeter volume of the brain (Fig. 1C). EM has been employed exten-
91 sively in large-scale datasets to map drosophila [23, 24], worm [25], mouse [26, 27], and

V1 Deepdive: Large-Scale Multi-Modal Data

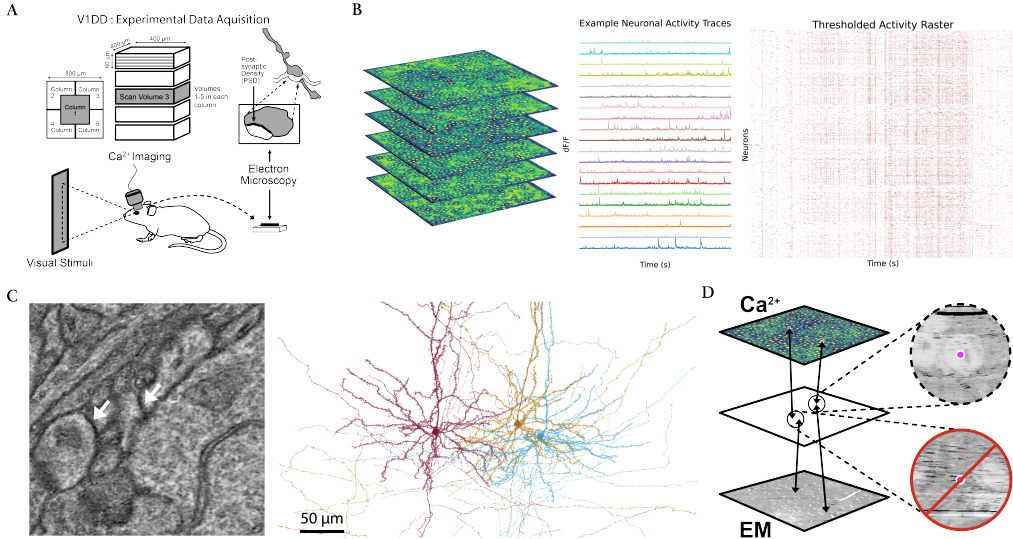


Figure 1: **(A)**. Schematic of experimental data acquisition for the V1 Deepdive dataset (V1DD). V1DD consists of dense thousands of excitatory neurons in an $800 \times 800 \times 800 \mu\text{m}^3$ section of mouse V1, recorded during awake behaving imaging sessions, with no behavioral task. Our work focuses on the center column, particularly the third scan volume (pictured here in grey). Postmortem, the same tissue volume was fixed and imaged via transmission electron microscopy, allowing for reconstruction of synaptic connectivity, including post-synaptic density (PSD) volumes. **(B)** Each scan volume for in vivo imaging consisted of six stacked scan planes. Dense calcium activity allowed for the extraction of individual neuronal traces, with 20 example traces shown in addition to a raster plot of thresholded normalized activity for all 2708 neurons in Scan Volume 3 of Column 1. **(C)** Example of a microscopy view of connected neurons, with white arrows pointing to PSD. Reconstructed pyramidal cells corresponding to the left microscopy view are shown on the right. **(D)** Schematic showing the framework for coregistration of cells between the calcium recordings and the electron microscopy. Identified ROIs were mapped to an interstitial space (see Methods 5.1.4), where the correspondences were manually inspected.

even the human brain [28]. The combination of these two imaging modalities has been applied in very few datasets [29, 30, 27], particularly at this scale.

These advances offer the opportunity to examine the structural correlates of Hebbian cell assemblies at an unprecedented scale. We extract assemblies from a Ca²⁺ fluorescence imaging scan and examine the reliability of their activation and their functional significance in the encoding of visual stimuli. We then analyze the connectivity between neurons based on cells that were coregistered between fluorescence and structural EM scans (Fig. 1D). Deriving hypotheses directly from postulates advanced by Hebb, we test his predictions about synaptic sizes and connectivity within and across assemblies, producing results that suggest a significant role for inhibition in their formation and activation, different from what is traditionally assumed.

103 **3 Results**

104 **3.1 Neuronal Organization of Hebbian Assemblies**

105 We analyzed a scan of the optical imaging dataset consisting of 2708 excitatory
106 neurons recorded in parallel. The Similarity Graph Clustering (SGC) algorithm (Fig.
107 2A) generated 15 assemblies, which we ordered by size with ‘A 1’ representing the largest
108 assembly ($n = 1016$) and ‘A 15’ the smallest ($n = 23$). A subset ($n = 748$, 27.6 percent
109 of 2708 total) of neurons was assigned to no assemblies.

110 Their spatial distributions are shown in (Fig. 2C,D). Although spatial organization
111 is not clearly visible, statistical analysis using the Kolmogorov-Smirnov (KS) [31] test
112 revealed significant differences in the spatial organization of assemblies compared to
113 that of the entire neural space (Fig. 2E). In particular, there was marked organization
114 in nearly every assembly along the x-y plane, indicative of the retinotopic organization
115 observed in studies of the visual cortex [32].

116 Most, but not all, assemblies shared members with other assemblies (Fig. 2B).
117 For example, neurons assigned to ‘A 1’ were also assigned to ten other assemblies,
118 highlighting Hebb’s proposal that precisely timed phase sequences allow a set of shared
119 member neurons to participate in multiple assemblies.

120 **3.2 Correlation and Sparsity**

121 By construction, assemblies are expected to respond to distinct stimulus features,
122 with a coactivity correlation sufficiently low to prevent their merging into a single assem-
123 bly. Pearson correlation coefficients between assembly coactivity traces were significantly
124 lower than the coefficients between coactivity traces of random ensembles of the same
125 size distribution (see Methods) (Fig. 3A). As expected from traces derived from the
126 average of population raster activity, both populations were significantly higher in their
127 correlation than individual cell activity raster correlations, regardless of the subset of
128 pyramidal cells being considered (assembly, non-assembly, or all individual cells).

129 To further characterize the functional properties of assemblies, we computed the Gini
130 coefficient [35] for each assembly’s activity trace. The Gini coefficient, a statistical mea-
131 sure of the ‘inequality’ of signal activity throughout the optical recording, revealed that
132 assemblies exhibited highly sparse activity patterns (Fig. 3B), exhibiting significantly
133 higher Gini coefficients than random ensembles (p -value : $6.23e - 5$). The coefficient for
134 each assembly ranged from 0.55 to 0.83, with particular assemblies with extreme spar-
135 sity, such as ‘A 13’ (0.79) and ‘A 15’ (0.83), exemplifying a high degree of functional
136 selectivity. Interestingly, this sparsity metric was not solely dependent on assembly size,
137 as intermediate-sized assemblies (e.g., ‘A 4’ through ‘A 12’) all exhibited similar Gini
138 coefficients of around 0.70.

139 **3.3 Assemblies Reliability in Stimuli Response**

140 A section of the visual stimuli presented to the mouse consisted of natural movies.
141 Across the hour scan time, twelve unique 15-second movie clips were repeatedly shown
142 eight times. To evaluate the functional reliability of neuronal assemblies, we analyzed
143 their responses to these stimuli. Reliability was quantified using an Oracle score, a
144 leave-one-out correlation metric (see Methods 5.3) that measures the consistency of an
145 activity trace across repeated presentations of the same stimulus. Oracle scores have
146 been used as a measure of the reliability of neuronal response [36]. To provide a baseline
147 with which to compare the functionality of these assemblies to tune to visual stimuli,
148 the oracle scores of assemblies’ coactivity traces were compared to the oracle scores of

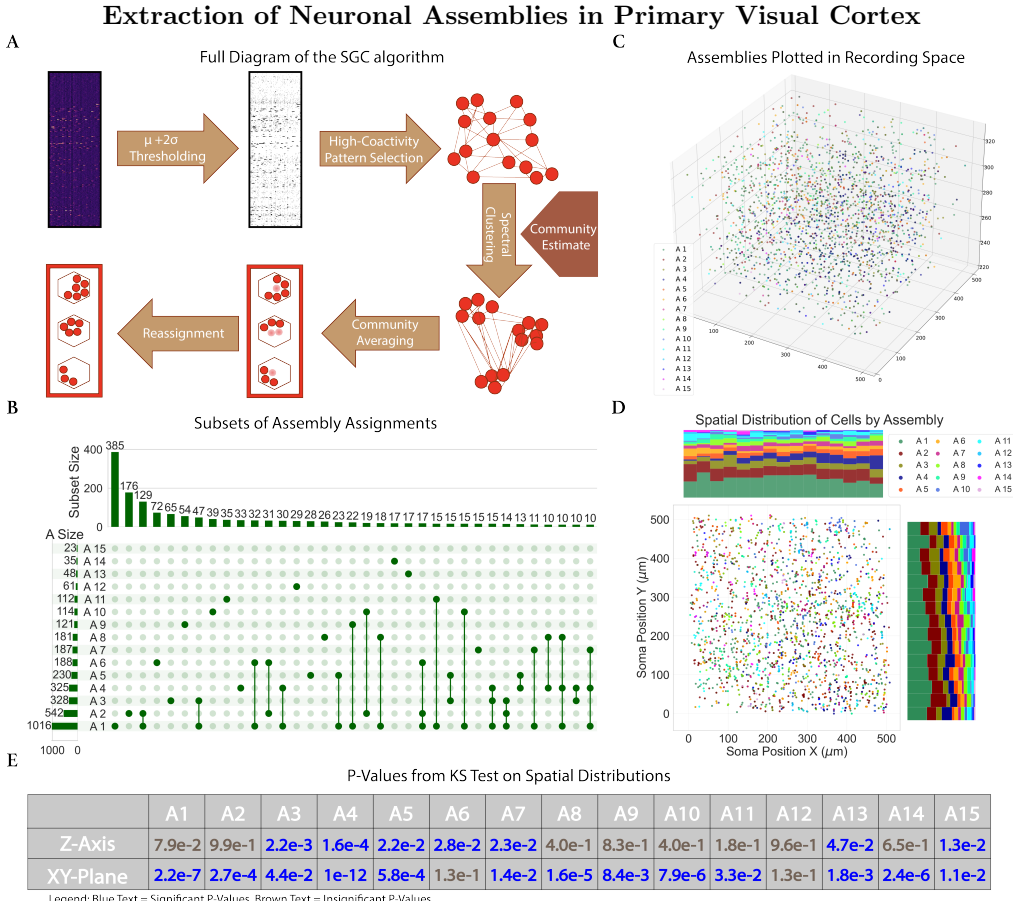


Figure 2: (A). SGC, an extraction algorithm for assemblies uniquely designed for calcium imaging data, groups frames of the calcium fluorescence input to determine when neurons in assemblies are coactivated. Figure adapted from Mölter et al. [33] (B). An UpSet [34] visualization of the subsets formed between assembly assignments. The histogram on the left represents the size of each individual assembly. The top histogram represents the size of the subsets between assemblies. Only subsets of ten neurons or greater were visualized. (C). Spatial positions of fifteen extracted assemblies in the three-dimensional recording field. There are 1960 neurons visualized, including neurons assigned to multiple assemblies (plotted only once) but not including the 748 neurons that were assigned to no assemblies. (D). Spatial distribution of assembly cells projected onto the x-y plane. Histograms for each axis are normalized to provide a per-bin proportional stack of the assembly distributions. (E). A table presenting the KS test results on each assembly's spatial distributions. Values colored in blue represent significant results ($p\text{-value} < 0.05$), while brown signifies insignificant results.

149 all neuronal traces. In addition, we provide a population-level comparison with random
150 ensembles.

151 Assemblies exhibited significantly higher Oracle scores compared to the average re-
152 liability of individual neurons (p -values < 0.0001), indicating that the assemblies, as
153 populations, respond more consistently to visual stimuli (Fig. 3C). To ensure this
154 result was not merely due to the inclusion of highly reliable neurons within assem-
155 blies, we separately calculated Oracle scores for neurons within assemblies and those
156 assigned to no assemblies. We observed no significant difference between the cellular
157 sets (p -values > 0.25). This result suggests that the reliability of these assemblies is
158 derived from their collective activity rather than from the reliability of individual mem-
159 bers.

160 Since population coactivity is expected to be more reliable in the general case than
161 individual neurons, we compared our assemblies to random ensembles (defined as in
162 Methods 5.2). Assembly coactivity traces demonstrated higher Oracle scores than coac-
163 tivity traces computed in the same way as the assemblies for size-matched random
164 ensembles. Complementary results are seen in the reliability of responses to orienta-
165 tion gratings (see Supp. Fig. 6). Population activity during the presentation of these
166 gratings was used to characterize reliability as a function of orientation [37].

167 Further analysis revealed consistent patterns of high assembly coactivity during spe-
168 cific visual frames of these natural movies. We defined ‘trigger frames’ as moments when
169 assembly activity exceeded a baseline threshold (see Methods 5.2) and found that these
170 frames were highly consistent across repeated stimulus presentations. Example mean
171 trigger frame pixel values are presented in (Fig. 3F), along with those of the corre-
172 sponding size-matched random ensemble, and the squared difference. Visualizations of
173 these frames suggest that assembly activity responds to complex features in the natu-
174 ral movies. These collective results provide evidence of assemblies’ ability to serve as
175 functional populations with reliable and specific responses to visual stimuli.

176 3.4 Decoding Responses from Acute Visual Stimuli

177 We also assessed the ability of assemblies to decode visual stimuli by implementing
178 a classification framework comparing assemblies to random ensembles (Fig. 3D, E). We
179 employed a Multi-Layer Perceptron Classifier (MLPClassifier) to evaluate how well each
180 grouping could decode the identities of the twelve natural movie clips. These classifiers
181 have been shown to be effective in academic and clinical settings, with high levels of
182 accuracy and flexibility in available hyperparameters [38, 39].

183 The results of our classifier revealed that assemblies significantly outperformed ran-
184 dom ensembles in accuracy. Heatmaps of classification accuracy for natural movie clip
185 identities demonstrated that assemblies provided more reliable decoding across repeated
186 trials. A Mann-Whitney U-test confirmed this finding, with assembly accuracy signifi-
187 cantly exceeding random ensembles for both overall performance (u -stat: 7546.0 p -value:
188 $6.06e - 5$) and diagonal elements (one-sided, u -stat: 131.5 p -value: 0.00032), indicating
189 enhanced stimulus-specific decoding.

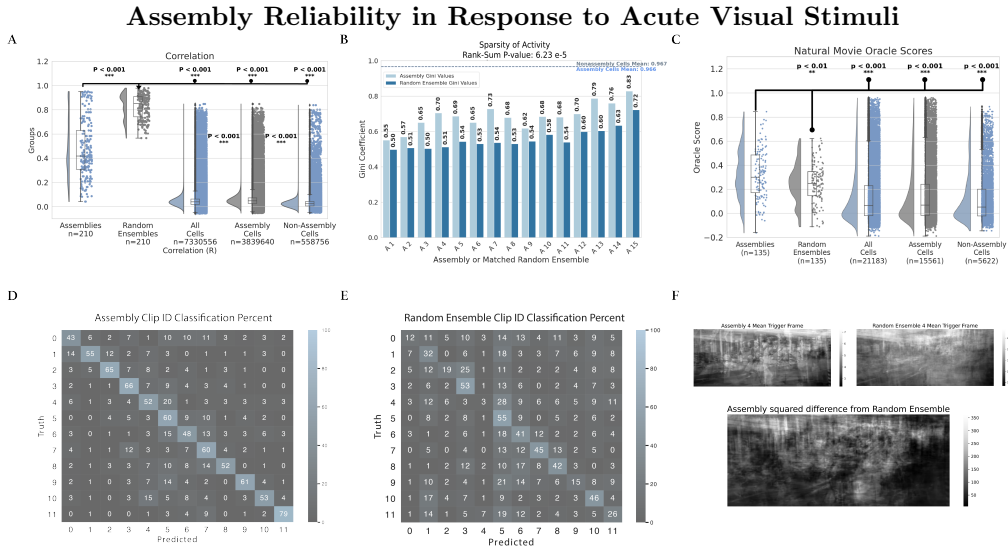


Figure 3: **(A)** Raincloud plot of pairwise correlations of coactivation between assemblies, size-matched random ensembles, and sets of individual cells. Coactivation for an individual cell is equivalent to a binary thresholded activity raster. **(B)**. Grouped bar plot of sparsity (measured by the Gini Coefficient) of coactivity over time in cell assemblies and the null-grouping of size-matched random ensembles. The random ensembles' coefficients are significantly smaller than the set of assembly coefficients (Wilcoxon Rank-Sum p-value: $6.234e - 5$). The average sparsity of individual assembly cells and non-assembly cells is also plotted as nearly equal horizontal dashed lines. **(C)**. Raincloud plot illustrating the reliability of activity from assemblies and general neuronal populations in response to natural movies. Oracle scores of each assembly and random ensemble coactivity trace were plotted, as well as the scores of sets of individual cells. These oracle scores are computed for the concatenation of natural movie clips and their responses, rather than individual clips, in order to reduce the likelihood of sparse responses causing an artificially high reliability score. **(D, E)**. Heatmap illustrating decoding accuracy of natural movie clips with Assemblies and Random Ensembles. Heatmap values indicate the accuracy of clip decoding by the percentage of presentation. Clip IDs, indicating a unique natural movie clip, are balanced such that each clip has an equal frequency of presentation. Values in the assembly heatmap are significantly greater than the random ensemble heatmap (Mann-Whitney u-stat: 7546.0 p-value: $6.06e - 5$, one-sided on diagonal elements u-stat: 131.5 p-value: 0.00032). **(F)**. Example plots of the mean ‘trigger frame’ of assemblies and random ensemble during natural movies. Frames were generated by averaging the frames associated with peak coactivity. The natural movie frame was visually better reconstructed by the assembly activity than that of the random ensemble, as signified by the plotted squared difference.

190 3.5 Structural Organization of Assemblies

191 Coregistration between recorded activity and EM data provides us with a unique
 192 opportunity to explore the structural underpinnings of assemblies in the visual cortex.
 193 By mapping neural structure and connectivity at a micrometer resolution, we investi-
 194 gated the anatomical communication and organization of neurons with at least one
 195 shared assembly membership (shared assembly cells) compared to those with disjoint
 196 membership.

197 The strength of connections between the two groups was measured by performing a

198 Wilcoxon Rank Sum test to compare the connection weights (defined as the sum of PSD
199 volumes for all synapses between two cells). A Chi-squared test of Independence was
200 performed to determine whether the pairwise frequency of connections differed between
201 cells with shared assembly membership and those with disjoint assembly membership.
202 To investigate higher-order structural patterns, we performed similar tests on sets of
203 inbound and outbound disynaptic chains, as well as subdividing based on whether the
204 intermediate cell in each chain was inhibitory or excitatory. 5.11.2

205 Our initial analysis of first-order connectivity surprisingly revealed no significant
206 differences in the probability of direct monosynaptic connections between shared and
207 disjoint sets or the strengths of those connections (Fig. 4D,E). This finding is incongruous
208 with predictions that assemblies are defined by densely interconnected excitatory
209 neurons [1] and suggested that the defining structural characteristics of assemblies might
210 lie beyond simple pairwise connectivity metrics.

211 To investigate higher-order structural patterns of these assemblies, we conducted a
212 motif analysis. In a neural network, when a significant number of subgraphs containing
213 a small number of interconnected cells repeat a particular pattern (e.g., Cell Type A →
214 Cell Type B → Cell Type A), they are classified as a motif [40, 41], with each subgraph
215 counted as a motif instance. The frequency with which these motifs persist has been
216 predictive of correlation in similar neural networks [42].

217 Our analysis concentrated on second-order chain motifs, or structures consisting of
218 three neurons connected by two synaptic links (schematic shown in Fig. 4F,H). Second-
219 order neural motifs are divisible into various types based on the arrangement of their
220 synaptic connections. For this study, we prioritized chain motifs, as they allowed us to
221 utilize aspects of the EM dataset that are not yet coregistered to activity recordings
222 for the central elements in the chain, so long as the first and last cells in the chain are
223 coregistered.

224 Notably, while our excitatory chain analysis revealed no significant differences be-
225 tween shared and disjoint assembly memberships (Fig. 4F,G), an analysis of inhibitory
226 motifs convey a different story: disjoint assembly memberships exhibited significantly
227 stronger feed-forward inhibitory connections than shared memberships (Fig. 4H,I). Log-
228 scaled plotting of the chain weights (Fig. 4I, inset) revealed a complete lack of overlap
229 between SEM-based confidence intervals, suggesting that this is a result with both reliabil-
230 ity and a non-trivial effect size. Notably, this result was insignificant when restricting
231 our analysis to only the inhibitory synapse or only the excitatory synapse within the
232 feed-forward inhibitory chain, suggesting that both connections may play a role.

233 The significantly stronger feed-forward inhibitory connections suggest a mechanism
234 of mutual inhibition that may regulate the interaction between distinct assemblies, pre-
235 venting excessive coactivation and ensuring the discriminability of assembly responses
236 to inbound information. Indeed, we find a negative Pearson r correlation coefficient be-
237 tween the disjoint feed-forward inhibitory chain weights and the correlation of the two
238 disjoint assemblies' coactivity traces (r statistic : -0.19, p -value : 0.0048; see Methods
239 5.11.4).

240 All together, our structural results reveal that assemblies are not anatomically de-
241 fined solely by a fundamental increase in local connectivity, but through their higher-
242 order patterns of organization. Stronger feed-forward inhibitory connections in disjoint
243 memberships suggest a possible mechanism for maintaining functional segregation be-
244 tween assemblies. These structural insights provide intuition on the mechanistic basis
245 that drives the functional properties of assemblies, reinforcing their contribution as mod-
246 ular units of sensory processing.

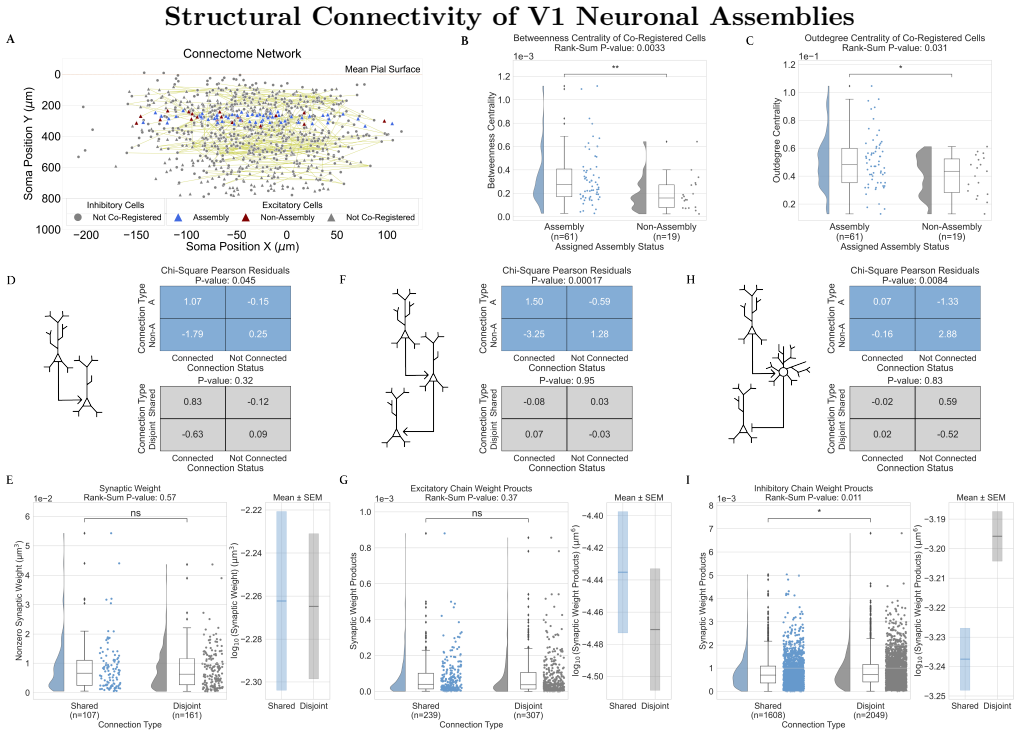


Figure 4: **(A)**. Visualization of the network being analyzed, showing the soma position of cells in the connectome, colored by cell-type and assembly assignment. All coregistered reconstructed neurons were found in layer 2/3 or layer 4 of V1. **(B)** A raincloud plot of betweenness centrality, demonstrating a higher centrality for assembly neurons than those not in assemblies(Wilcoxon Rank-Sum: p-value < 0.01). **(C)** A raincloud plot of outdegree centrality, a mathematical proxy for probability of connection, demonstrating a higher centrality for assembly neurons (Wilcoxon Rank-Sum: p-value < 0.05). **(D,F,H)**. Chi-squared analysis of the likelihood of monosynaptic (D), disynaptic excitatory (F), and disynaptic inhibitory (H) connections (schematic on the left). This comparison was made between assembly neurons and non-assembly neurons (top-right) as well as between neurons that share an assembly membership and neurons that participate in disjoint assemblies (bottom-right). **(E, G, I)** Raincloud plots showing the combined synaptic PSD volume per extant monosynaptic (E), disynaptic excitatory (G), and disynaptic inhibitory (I) connection, each divided between origin and terminus cell pairs which share assemblies and those which participate in disjoint assemblies. Log-scaled plotting of the chain weights with SEM-based confidence intervals is included as an inset plot to the right of each panel.

247 3.6 Non-Assembly Cells

248 The same monosynaptic and disynaptic analysis run on pairs of cells with shared
 249 assembly memberships and cells with disjoint memberships was also run on pairs of
 250 assembly cells (cells that both participate in at least one assembly) and pairs of non-
 251 assembly cells (cells that had no assembly memberships for either cell).

252 We show assembly cells exhibiting a pattern of connectivity distinct from non-
 253 assembly cells, a requirement of Hebb's theory. We assessed the higher-order integration
 254 of assembly neurons into the broader structural network using centrality metrics.
 255 In particular, we found significantly lower betweenness centrality (Fig. 4B), a measure

256 of a node's importance in mediating communication within a network, and outdegree
257 centrality (Fig. 4C), an analog for probability of outbound connectivity, in neurons
258 outside assemblies compared to neurons within assemblies. Furthermore, we found that
259 the pairwise probability of monosynaptic connections, disynaptic excitatory chains, and
260 disynaptic inhibitory chains was significantly greater for cells sharing assembly member-
261 ship than for non-assembly cells (p-values : 0.045, 0.0002, and 0.0084, respectively). No
262 significant differences in PSD Volumes between assembly and non-assembly cells were
263 observed. These findings confirm that cells in the connectome participating in at least
264 one assembly are more interconnected than those not participating in any.

265 Overall, these results indicate reduced participation in the structural framework of
266 the primary visual cortex for non-assembly cells and imply an organizational role of
267 assembly neurons as hubs for information flow. In contrast, non-assembly neurons may
268 play a more peripheral, secondary role in the network, such as noise filtering.

269 4 Discussion

270 4.1 Inhibition as the Delineating Basis of Hebbian Assemblies

271 This work provides the first demonstration of the structural underpinnings of Hebb-
272 ian assemblies and validates Hebb's assembly theory in a surprising way; while there is
273 strong agreement on functional predictions, our structural findings run counter to Hebb's
274 original proposal. We do not observe a marked increase in the strength or probability of
275 excitatory connections between cells that participate in the same assembly (Fig. 4D-G).
276 Instead, we find significantly stronger feed-forward inhibitory connections targeting cells
277 in other assemblies (Fig. 4I). Hebb and others [43, 9, 3] have hypothesized that targeted
278 inhibition could play a crucial role in the formation and delineation of assemblies. Our
279 findings offer the first clear empirical evidence for this mechanism.

280 Despite this novel result, our findings remain a validation of Hebb's structural pos-
281 tulates and are consistent with what would be required for assemblies to be delineated
282 by inhibition. Assembly cells were substantially more integrated into the connectome,
283 displaying significantly higher betweenness and outdegree centrality (Fig. 4B,C). This
284 pattern demonstrates that cells participating in our activity-defined assemblies possess
285 markedly different patterns of connectivity from cells that do not, establishing the nec-
286 essary structure-function relationship postulated by Hebb.

287 Intuitively, the delineation of assemblies can be realized on a spectrum between in-
288 ternal (shared-assembly) excitation and external (disjoint-assembly) inhibition. Shared-
289 assembly excitation would rely on broad inhibitory connectivity across the entire pop-
290 ulation of assembly neurons, and disjoint-assembly inhibition would similarly rely on
291 broad excitatory connectivity. We find a significantly greater probability of excitatory
292 connections between cells belonging to any assembly (Fig. 4D,F), however we did not
293 observe significantly stronger or more frequent excitatory connections between neurons
294 with shared assembly membership (Fig. 4D-G). Combined with our finding of signifi-
295 cantly greater feed-forward inhibitory weights between neurons with disjoint assembly
296 membership (Fig. 4I), the broad excitation strongly suggests that the extracted assem-
297 blies are delineated predominantly via inhibition.

298 4.2 Functional Consistency of Assemblies

299 Functionally, ensembles of cells classified as assembly cells behave in ways consistent
300 with Hebbian assemblies. The assemblies demonstrated markedly higher reliability in
301 their responses to naturalistic visual stimuli compared to individual cellular responses
302 of all three sub-populations of cells and size-matched random ensembles, reflected by

303 significantly elevated Oracle scores (Fig. 3C). This consistent coactivity of the assemblies
304 has been hypothesized to offer resilience to representational drift, allowing them to
305 serve as a substrate for long-lasting representation [8]. Representational drift reflects a
306 functional characterization of fluctuations at the cellular level, such as synaptic turnover
307 [44, 45], even under stable stimulus conditions [46]. This phenomenon has been observed
308 in areas other than V1, such as the piriform cortex [47]. By maintaining consistent and
309 coherent patterns of coactivity, assemblies may offer a general cortical mechanism of
310 stable perceptual representations despite such turnover.

311 Beyond their reliability in responses, assemblies were also superior in our decod-
312 ing of natural movie presentations (Fig. 3D), underscoring their efficacy in extracting
313 higher-order visual information. In addition, the sparsity of assembly coactivity was
314 substantially greater than that of random ensembles (Fig. 3B), which, when combined
315 with a lower average correlation 3A), is consistent with assemblies employing a cost-
316 effective encoding strategy [48]. Such a strategy would enhance the capacity for distinct
317 representation of sensory inputs, translating more flexible individual responses into reli-
318 able population-level encoding. Finally, cells assigned to assemblies exhibit significantly
319 higher pairwise correlations than non-assembly cells, corroborating the experimental
320 work of Harris and Carandini [49] defining ‘choristers’ and ‘soloists’. However, we found
321 no difference in their average response reliability to natural movies or in their overall
322 signal sparsity. This result implies that a population perspective is required for the
323 encoding of reliable perceptually relevant stimulus features.

324 **4.3 Connective Tissue of Structure and Activity**

325 Some examined ensemble features bridge structure and activity, a crucial aspect of
326 this study, which has not previously been achievable at scale. First, the extensive overlap
327 of neurons across multiple assemblies (Fig. 2D) is consistent with both Hebb’s proposal
328 of sub-assemblies [9] and Yuste’s review of definitions put forward for ensembles [50],
329 with individual neurons contributing to multiple functional modules. Second, our ob-
330 servation of greater chain weights in feed-forward inhibitory chains offers a mechanistic
331 explanation of how assemblies can retain distinct responses to stimuli without becoming
332 so correlated in their activity that they merge into a single functional ensemble. The
333 plausibility of this explanation is supported by the significant observed negative cor-
334 relation between inhibitory chain connection strength between disjoint assemblies and
335 the r coefficient of their paired assembly coactivity traces, showing that the greater the
336 inhibitory weight of the connections observed, the less correlated the activation of the
337 two assemblies is 3.5.

338 **4.4 Further Directions**

339 Looking ahead, assemblies exhibit notable variability in size (Fig. 2D). SGC min-
340 imizes overestimation of the number of assemblies or neuron assignments, suggesting
341 that these size differences reflect intrinsic properties rather than methodological arti-
342 facts. There is therefore an opportunity for future studies to delineate the distinct roles
343 potentially served by larger assemblies, such as ‘A 1’, compared to their smaller counter-
344 parts. In addition, while novel in its scale and multifaceted nature, we see opportunities
345 to reduce some of the current limitations within this dataset. Continued reconstruction,
346 proofreading, and coregistration will allow analyses of more neurons and subsequent
347 new lines of inquiry. For instance, the SGC algorithm flags frequent patterns of ac-
348 tivity, potentially analogous to Hebbian phase sequences [6, 7]. We currently do not
349 have sufficiently many coregistered and fully reconstructed cells to allow examination
350 of connections that bridge one pattern to the next. Exploring how these patterns inter-

351 act could reveal mechanisms of large-scale neural coordination. Other limitations will
352 be more difficult to overcome without the availability of next-generation multi-modal
353 datasets. Most importantly, the temporal resolution of the scans leaves us with no ability
354 to examine activity on some of the most relevant time scales for synaptic plasticity.

355 These results suggest several potential implications for the field at large. Hebb pro-
356 posed assemblies as a universal building block, simultaneously addressing the functional
357 and structural sides of perception, cognition, and behavior. A basic unit that bridges
358 structure and function allows one to derive structural predictions from functional char-
359 acterizations and vice versa. Beyond validating Hebb's theory, the evidence presented
360 here for an underlying inhibitory mechanism provides further support for the analysis of
361 inhibition in cognitive and sensory disorders studied to date primarily through the lens
362 of excitation [51, 52]. In the future, the integration of cell-type-specific genetic informa-
363 tion with functional assembly data could also provide deeper insights into the molecular
364 foundations of assembly formation and maintenance in health and disease [53]. Hebb
365 postulated that assemblies form the atoms of cognition, and it has not escaped our
366 notice that the cross-inhibitory mechanism we here demonstrate might be a universal
367 feature of brain-wide assembly organization.

368 **5 Methods**

369 **5.1 V1 Deepdive Dataset**

370 **5.1.1 Stimuli**

371 Visual stimuli were presented using the same monitor configuration as in de Vries
372 et al. [54]. Imaging sessions were one hour long and offered a wide variety of visual
373 stimuli. Assembly extraction was performed on the fluorescence data from the full
374 session. The remainder of our analysis utilizes only the natural movie clips and the full-
375 field drifting gratings, details of which are provided below. The other stimuli presented
376 during the session included natural images, windowed drifting gratings, and locally
377 sparse noise. The details of these other classes of stimuli can be found in [21]. The
378 natural movies stimulus consisted of 3,600 frames (with 30 Hz frame rate), presented 8
379 times. The full-field drifting gratings stimulus consisted of a drifting sinusoidal grating at
380 a 1 Hz temporal frequency and 80 percent contrast, presented at 12 different orientations
381 (multiples of 30°) and at 2 spatial frequencies (0.04 and 0.08 cycles per degree). Each
382 condition was presented eight times, in randomized order, with one second of mean
383 luminance grey between presentations.

384 **5.1.2 2/3 Photon Microscopy and Activity Data Processing**

385 The full $800 \times 800 \times 800 \mu\text{m}^3$ volume was divided into five columns, each imaged via ei-
386 ther 2-photon (2P) or 3-photon (3P) microscopy, depending on depth. The volumes were
387 scanned over the course of several sessions. Each session consisted of the full set of visual
388 stimuli (see below), presented in the same order and with the same timing. Our anal-
389 ysis is concerned only with the central column, centered within the $800 \times 800 \times 800 \mu\text{m}^3$
390 volume, where the largest set of reconstructed, coregistered, and proofread neurons is
391 currently available. Figure 1A shows the arrangement of scan volumes (5 volumes span-
392 ning 75 μm to 620 μm depth, each $400 \times 400 \times 80 \mu\text{m}^3$) and imaging planes (6 planes
393 within each scan volume, separated by 16 μm at thirty-seven frames per second so that
394 each plane is imaged at 6 Hz.) We selected volume three of the central column for our
395 primary analyses and validated our work with volume four. Both were imaged with 2P
396 microscopy. Details on the other columns and the 3P imaging can be found in [21].

397 The fluorescence data was preprocessed using the standard LIMS pipeline as used
398 for the Allen Institute’s Visual Coding 2P dataset [54], including motion correction,
399 segmentation, demixing, neuropil subtraction, ROI filtering, and df/f calculation. Iden-
400 tified regions of interest were run through a classifier trained on manual labeling data
401 meant to reduce the false classification of artifact ROIs as neuronal somas, and only
402 those with a high confidence score (at least 0.5) were included in our analysis.

403 **5.1.3 Electron Microscopy and Reconstruction**

404 The mouse was transcardially perfused with a fixative mixture of paraformaldehyde
405 and glutaraldehyde. All procedures were carried out in accordance with the Institutional
406 Animal Care and Use Committee at the Allen Institute for Brain Science. The large-
407 volume staining protocol was adapted from [55]. After dissection, the neurophysiological
408 recording site was identified by mapping the brain surface vasculature. A thick (1200 μm)
409 slice was cut with a vibratome and post-fixed in perfusate solution for 12 to 48 h. The
410 tissue was then infused with heavy metals, dehydrated, and embedded in EMS Hard
411 Plus resin. After curing, the samples were epoxy cured to a stub. They were then
412 sliced and placed onto continuous tape by a ATUMtome Automated Tape Collecting
413 Ultramicrotome.

414 The continuous tape was fed into an automated high-throughput transmission electron microscopy pipeline[56]. Transmission electron microscopy is particularly well
415 suited for automated imaging and preserves very good x-y resolution at the expense
416 of some resolution on the vertical z-axis, and so specialized methodology was deployed
417 during reconstruction[57, 58]. Serial section alignment was performed through a contract
418 with Zetta A.I., followed by stitching [59, 56], segmentation, and automated reconstruction.
419 Proofreading of a subset of cells was performed under contract by Ariadne.ai.
420

421 Cell-type predictions were made for single-nucleus objects within 175 microns of the
422 centerline and with a nucleus volume greater than 218, based on dendritic skeleton fea-
423 tures adapted from [60]. Segmentation and annotation were stored in a CAVE database
424 for access via CAVEClient [61].

425 5.1.4 Coregistration

426 Manual coregistration was performed using the Fiji plugin BigWarp [62, 63]. A
427 structural scan of the vasculature was aligned with the two-photon imaging planes (max
428 intensity projection). Next, a downsampled EM image was aligned to this composite
429 using a thin-plate-spline transform based on manual landmarks. After initial alignment,
430 the transform was used to predict additional correspondences between two-photon ROI
431 centroids and segmented EM cells. Four hundred verified correspondences between a flu-
432 orescence imaging ROI with a high classifier score and a corresponding morphologically
433 typed EM-reconstructed cell passed manual inspection by two independent reviewers
434 and were included in this study. 315 of these correspond to cells whose fluorescence was
435 recorded in the scan we analyzed (volume three of the central column). Of these 315,
436 80 had axon reconstructions that were verified accurate by trained experts ('proofread')
437 to their maximal extension within the scan volume. Coregistration and reconstruction
438 are ongoing at the time of this writing, but the extant data already allow for a relation
439 of the physiology of neural data to its exact anatomy at an unprecedented level.

440 5.2 Graph Clustering for Assembly Extraction

441 To extract assemblies, we use the Similarity-Graph-Clustering (SGC) algorithm that
442 has been originally proposed for the detection of neural assemblies during spontaneous
443 activity in the zebrafish optic tectum [64]. The SGC algorithm identifies neuronal assem-
444 blies using ideas from graph theory by transforming the problem into one of community
445 detection on some graph in which assemblies correspond to distinct (graph) communi-
446 ties. Unlike traditional methods that rely on pairwise correlations between cells, SGC
447 groups frames of fluorescence indicative of significant coactivity [33]. These moments of
448 higher-order correlation are referred to as potential 'phase sequences', representing when
449 populations of neurons act cohesively as a closed circuit during assembly activation [65].

450 Importantly, by design, SGC allows cells to participate in multiple assemblies. As-
451 sembly overlap has been integral to assembly studies in the past [66]. Hebb originally
452 postulated that the shift between active assembly states could be what is colloquially
453 referred to as a 'train of thought' [1]. Our results revealed a sizable degree of overlap
454 between assemblies, which was visualized through an UpSet plot (Fig. 2D) [34], showing
455 neurons frequently assigned to multiple assemblies (Fig. 2D).

456 Compared with several other prominent assembly extraction algorithms upon appli-
457 cation to both simulated and biological calcium imaging datasets under different condi-
458 tions, this algorithm was shown to perform best overall [33]. Although it did not yield
459 a perfect reconstruction of the assemblies in the biological dataset, SGC was able to
460 recover the assemblies with higher accuracy than all other algorithms. In part, this per-
461 formance has been attributed to the computational effort that SGC places in estimating
462 the number of assemblies before defining them.

We used a recent implementation of the SGC algorithm in Python [67]. For completeness, we briefly recall the main steps here: The algorithm commences by thresholding the calcium fluorescence signals (df/f) of the ROIs (neurons) by two standard deviations above the mean to minimize noise (Fig. 2B). Afterwards, activity patterns are selected where the coactivity level of neurons exceeds the significance threshold. This threshold that determines the set of “high-activity patterns” is based on a null model of coactivity obtained from shuffling the thresholded activity signals (significance value: 0.05, rounds: 1000). A k -nearest-neighbor graph is then constructed from the set of high-coactivity patterns based on the similarity between the patterns in the cosine distance. For that, the number of neighbors k is automatically chosen such that the resulting graph is connected. In the next step, the number of communities in this graph is estimated using a statistical inference procedure. For our study, we fixed the hyperparameters with five independent Monte Carlo rounds of 150,000 steps each. With an estimate for the most likely number of communities, spectral clustering is applied. These clusters of high-coactivity patterns are the first prospective selection of coactivity patterns corresponding to the assemblies. However, the final step is a combination of averaging and reassignment to reject groups that may have been erroneously defined because of a high level of noise in the original signal. This minimizes the likelihood of overestimating the number of assemblies or the neurons that should be assigned to those assemblies. Neurons are assigned to assemblies based on their affinity, the probability that they were active in any of the assemblies’ activity patterns (affinity: 0.4). To establish our hyperparameters, we first performed a grid search on an independent functional scan volume (Scan Volume 4, acquired under identical conditions). Candidate values of Monte Carlo rounds, activity thresholds, and affinity cut-offs were evaluated by how well the resulting assembly assignments could fit to a low-dimensional embedding of pairwise activity correlations (see Supp. Fig. 7). The parameters that maximized the AIC value were rounds = 150,000, Z = 2 sd, and affinity = 0.4. These parameter values were then locked and applied to scan volume 3.

5.3 Random Ensembles

Random ensembles served as a null model and were defined as randomly selected sets of neurons drawn with equal probability and no replacement from the population of all recorded pyramidal cells within scan volume 3. Each set was size-matched to its corresponding assembly, with the same number of neurons.

5.4 Oracle Scores

Oracle scores are a measure of the reliability of the trace response of cell activity to repeated visual stimuli computed through a jackknife mean, or leave-one-out mean [68, 69], of correlations between the activity trace across the repeated visual stimuli. In this work, we treat the entire stereotyped stimulus sequence as a single stimulus, concatenating natural movie clips and their responses, rather than calculating the score for individual clips. This should reduce the risk of sparse responses leading to an artificially high reliability score.

Let $S_i(t)$ denote the activity trace of a neuron or an assembly during the i -th presentation of a stimulus at time t . Let $\bar{S}_{-i}(t)$ represent the mean activity trace of all activity traces excluding the i -th presentation, out of n total presentations of the same stimulus. From this, we can calculate the Oracle score O as

$$O = \frac{1}{n} \sum_{i=1}^n \frac{\text{Cov}(S_i(t), \bar{S}_{-i}(t))}{\sqrt{\text{Var}(S_i(t)) \cdot \text{Var}(\bar{S}_{-i}(t))}}.$$

508 In this formulation, the numerator will calculate the covariance between the activity
 509 trace at each presentation to the mean activity of all other repeats, while the denomina-
 510 tor scales the magnitude of this covariance by the product of the standard deviations
 511 of $S_i(t)$ and $\bar{S}_{-i}(t)$.

512 5.5 Trigger Frames

513 To assess the visual stimuli associated with high activity in neuronal assemblies,
 514 we computed trigger frames by identifying peak activity times and extracting the corre-
 515 sponding images from a natural movie presentation. From a coactivity trace for assembly
 516 k over time $S_k(t)$, we can detect peaks P_k using the `scipy` signal package to define local
 517 maxima. We then define a mean trigger frame $\mu_k(x, y)$ for a pixel (x, y) as

$$\frac{1}{|P_k|} \sum_{t \in P_k} I_t(x, y)$$

518 where $I_t(x, y)$ is the natural movie frame at time t .

519 This allowed us to visualize the average triggering frame for each assembly. The
 520 same process was then repeated for the coactivity traces of the size-matched random
 521 ensembles, and the squared difference between the average frame for each assembly and
 522 the average frame for its corresponding random ensemble. These computations allowed
 523 us to determine which frame of visual stimuli and consistent features in those stimuli
 524 were most strongly associated with high assembly coactivity in particular, not merely
 525 broad neuronal activation.

526 5.6 Decoder

527 To evaluate the ability of assemblies to decode visual stimuli, we implemented a
 528 Multi-Layer Perceptron Classifier (MLPClassifier) from the `scikit-learn` library. This
 529 classifier was used to differentiate between 15 natural movie clips based on assembly
 530 coactivity time traces. Random ensembles of neurons with the same size distribution as
 531 the assemblies were used as a null model for comparison.

532 The MLP is a classical feed-forward neural network composed of an input layer, one
 533 or more hidden layers, and an output layer. Each node in a layer is fully connected to
 534 every node in the subsequent layer through weighted connections. The final output of
 535 the function is determined by a non-linear activation function applied to the weighted
 536 sum of its inputs plus a bias term.

537 The MLPClassifier from `scikit-learn` is an implementation of a Multi-Layer Per-
 538 ceptron (MLP), a type of feed-forward neural network. It operates by mapping input
 539 features \mathbf{x} to outputs $\hat{\mathbf{y}}$ through a series of hidden layers. Each layer consists of neurons
 540 that perform a weighted sum of their inputs, followed by the application of a non-linear
 541 activation function. Defining $\mathbf{W}^{(k)}$ as the weight matrix for the k -th layer, $\mathbf{h}^{(k)}$ as
 542 the input, and $\mathbf{b}^{(k)}$ as the bias vector for the k -th layer, we can define with activation
 543 function σ

$$\mathbf{h}^{(k)} = \sigma \left(\mathbf{W}^{(k)} \mathbf{h}^{(k-1)} + \mathbf{b}^{(k)} \right).$$

544 For classification, the final layer uses the softmax activation function to output prob-
 545 abilities for each class. With L denoting the number of layers, we can define these output
 546 probabilities as

$$\hat{\mathbf{y}} = \text{softmax}(\mathbf{h}^{(L)}) = \frac{\exp(\mathbf{h}^{(L)})}{\sum_j \exp(\mathbf{h}_j^{(L)})}.$$

547 The MLPClassifier is trained using backpropagation, optimizing the weights and
548 biases via stochastic gradient descent or adaptive solvers such as Adam. Regularization
549 can be applied through an ℓ_2 -penalty term, controlled by a hyperparameter.

550 The assembly coactivity time traces were paired with corresponding natural movie
551 clip IDs. The data was split into training and test sets using an 80-20 split, and features
552 were scaled to normalize the input. A cross-validated grid search was used to optimize
553 the hyperparameters.

554 5.7 Gini coefficient

555 The Gini coefficient [35], a statistical measure that exemplifies the state of inequality
556 within a population. While often applied in economics to evaluate income inequality,
557 this metric has been applied as a valid approximation for signal sparsity [70, 71]. This
558 rendition of the application has been shown to serve as a relatively simple and robust
559 measure [72]. For our study, the coefficient is employed to quantify assembly signal
560 heterogeneity.

561 The Gini coefficient, G is often calculated with respect to the Lorenz curve, which
562 plots the cumulative distribution of a set (e.g., assembly coactivity trace) against its
563 rank in ascending order. For a given assembly A with coactivity trace $S = [s_1, s_2, \dots, s_T]$
564 where s_t is the proportion of active neurons at time point t , the coefficient for that
565 assembly is then calculated as

$$G_A = \frac{\sum_{i=1}^{T-1} \sum_{j=i+1}^T |s_i - s_j|}{T^2 \cdot \bar{s}}.$$

566 This computation is performed independently for each assembly, providing a metric
567 of signal inequality. A value of 0 for G_A implies all values are identical, while a value
568 of 1 indicates perfect inequality *i.e. in a time series a single time point contains all the*
569 *activity*. A high value of G_A indicates that coactivity is dominated by a small number
570 of time points, reflecting the temporal sparsity.

571 5.8 Correlation

572 We examine coactivity correlations for each pair of assemblies, each pair of ran-
573 dom ensembles, and each pair of neurons within each of our three sets of neurons (see
574 Fig. 3A-C). To do so, we computed the Pearson's correlation coefficient r between the
575 two coactivity traces (where the coactivity trace of a single neuron is mathematically
576 equivalent to its thresholded raster activity, per [33]).

577 5.9 Motif Extraction

578 Motifs were extracted with the DotMotif Python package which detects subgraphs
579 within a graph based on the principle of subgraph monomorphism. For every graph
580 $H = (N_1, E_1)$ given by the user, the Dotmotif algorithm detects subgraphs G' within
581 the graph $G = (N_2, E_2)$ such that there exists a mapping $f : N_1 \rightarrow N'_2$ where $N'_2 \subseteq N_2$
582 and for every edge $(a, b) \in E_1$, the corresponding edge $(f(a), f(b)) \in E'_2$. The matched
583 subgraphs may also contain additional edges within the graph G . This algorithm was
584 used to detect disynaptic chains within the connectome.

585 To further refine our analysis, chain motifs were classified according to the type of
586 intermediary neuron, distinguishing between excitatory and inhibitory connections, with
587 the latter providing insight into feed-forward inhibition mechanisms.

588 **5.10 Motivating Postulates**

589 Our statistical analyses involve tests of the following postulates. First, excitatory
590 connections between cells that share at least one assembly ('shared' connections) will
591 be stronger than connections between cells which do not participate in any of the same
592 assemblies ('disjoint' connections), due to Hebbian plasticity [1]. This was examined
593 both with regard to the post-synaptic density volume of monosynaptic connections be-
594 tween known coregistered cells within the dataset, and separately in the form of the
595 product of connection PSD volumes in disynaptic excitatory chains which originated
596 and terminated with shared or disjoint cells, allowing us to evaluate indirect excitatory
597 connections where the middle cell had not yet been coregistered.

598 Second, that excitatory connections will be more frequent within assemblies than
599 between assemblies, due to a combination of Hebbian plasticity and pruning of synapses.
600 A number of computational studies have shown that long-term potentiation [73] and
601 pruning [74] play important roles in effective Hebbian assembly formation. This was
602 examined in the form of per-connection targeting statistics, as well as per-cell inbound
603 and outbound probability of both monosynaptic and disynaptic shared and disjoint
604 connections.

605 Third, as discussed in the introduction, Hebb himself suggested that the assem-
606 blies could have been formulated via modulation of inhibition. Additionally, a number
607 of computational models [75] have relied on inhibition between assemblies to restrict
608 simultaneous activation, enabling competition between assemblies. It was, therefore,
609 taken as an established hypothesis that one would expect inhibition between assemblies
610 to be greater than within a given assembly. As monosynaptic connections between ex-
611 citatory cells cannot be used to evaluate inhibition, this postulate was examined only in
612 disynaptic chains, where the middle cell was morphologically classified as an inhibitory
613 interneuron. Our examination involved the product of connection PSD volumes in such
614 disynaptic inhibitory chains bridging shared and disjoint assembly neurons, along with
615 a per-cell evaluation of the inbound and outbound probabilities of disynaptic inhibitory
616 chain connections.

617 Fourth, and finally, we acknowledge that Hebb discusses the reinforcement of sparse
618 connectivity in his accounts of the emergence of cell assemblies [43], and thus this re-
619 inforcement might have a significant effect on a sparse subset of connections while pro-
620 ducing a minimal difference in the central tendency of the overall set of connections.
621 Dorkenwald et al. [76] demonstrated a bimodality of the log PSD volume of excitatory-
622 excitatory synapses in the similar MICrONS mm³-dataset [27] (see also Supp. Fig.8 for
623 result in V1DD), suggesting that a subset of such connections is impacted differently
624 by processes determining PSD volume. Combining these two, we decided to test the
625 hypothesis that the larger of the two-component distributions found in [76] would be
626 more likely than chance to involve connections between shared assembly neurons.

627 **5.11 Statistical Methods**

628 In this section, we detail the motivations and specifics of our analysis and methods.

629 We analyzed differences in connectivity metrics between shared-assembly and disjoint-
630 assembly connection types, focusing on both the probability and strength of connections.
631 Our analysis considered both direct monosynaptic and disynaptic connections between
632 neurons ("by connection"), as well as the sets of inbound and outbound connections
633 grouped by cell ("by cell"). For disynaptic chains, we grouped by whether the interme-
634 diate (middle) cell was excitatory or inhibitory.

635 To evaluate connectivity metrics, we first defined the connection types based on
636 assembly membership. Let A be the set of all assemblies, with A_i denoting the subset
637 of assemblies that include cell i . Formally,

$$A_i = \{a \in A \mid i \in a\}.$$

Using these subsets, we defined the following binary indicators to capture the assembly relationship between pre-cell j and post-cell i :

- Shared _{ij} = 1 if $A_j \cap A_i \neq \emptyset$
- Disjoint _{ij} = 1 if $A_j \cap A_i = \emptyset$
- Assembly _{ij} = 1 if $A_j \neq \emptyset$ and $A_i \neq \emptyset$
- Non-Assembly _{ij} = 1 if $A_j = \emptyset$ and $A_i = \emptyset$

5.11.1 Monosynaptic Metrics

We defined w_{ij} as the pairwise summed post-synaptic density (PSD) between pre-cell j and post-cell i , and b_{ij} as an indicator variable that takes the value 1 if at least one synapse exists between j and i and 0 otherwise. All metrics exclude autapses, as these were not reliably represented in the dataset ($j \neq i$).

The probability of monosynaptic outbound connection for a pre-cell j was calculated as the proportion of realized connections under a given connection type $C \in \{\text{Shared, Disjoint, Assembly, Non-Assembly}\}$, normalized by the total number of potential post-cell partners for that connection type,

$$b_{\text{out}_j,C} = \frac{\sum_{i|C_{ij}=1} b_{ij}}{|\{i \mid C_{ij} = 1, i \neq j\}|}.$$

Similarly, the probability of a monosynaptic inbound connection for a post-cell i was defined as

$$b_{\text{in}_i,C} = \frac{\sum_{j|C_{ij}=1} b_{ij}}{|\{j \mid C_{ij} = 1, j \neq i\}|}.$$

For connection strength, we computed the average realized summed monosynaptic outbound PSD for a pre-cell j as the total PSD across all post-cells satisfying the connection type C , normalized by the number of realized ($b_{ij} = 1$) connection under C ,

$$w_{\text{out}_j,C} = \frac{\sum_{i|C_{ij}=1} w_{ij}}{\sum_{i|C_{ij}=1} b_{ij}}.$$

Similarly, the average realized summed monosynaptic inbound PSD for a post-cell i is given by

$$w_{\text{in}_i,C} = \frac{\sum_{j|C_{ij}=1} w_{ij}}{\sum_{j|C_{ij}=1} b_{ij}}.$$

660 **5.11.2 Disynaptic Metrics**

661 In examining the inhibition in sets of cells that share assembly membership, and
 662 in sets that do not, we were primarily interested in describing inhibition driven by
 663 the excitatory activity of an assembly's member cells. This moved us from the realm
 664 of monosynaptic connection analysis into an analysis of chains. Many aspects of our
 665 definition remained unaltered. A remained the set of all assemblies, with A_j the subset
 666 of assemblies that included pre-cell j , and A_i the subset of assemblies that included
 667 post-cell i . The binary indicators indicating the assembly relationship between cells i
 668 and j remained unaltered.

669 But rather than simply using the monosynaptic weight between neurons j and i
 670 where $j \neq i$, we defined w_{ikj} as the product of the pairwise summed post-synaptic
 671 densities w in a three-cell chain motif with j as the first cell, an interneuron k as the
 672 second cell, and i as the third cell. Thus,

$$w_{ikj} = w_{ik}w_{kj}.$$

673 And similar to our monosynaptic analysis, b_{ikj} was an indicator variable that took
 674 the value 1 if at least one disynaptic chain existed between j , k , and i and 0 otherwise.

675 Building on this definition, we outlined the method of normalization and metrics
 676 for disynaptic chain analysis, which accounted for both the intermediate and final (or
 677 first) cells in the chain. In this analysis, each pre-cell and post-cell was a coregistered
 678 excitatory neuron with an extended axon, consistent with the monosynaptic analysis.
 679 The intermediary cell in disynaptic chains, however, did not need to be coregistered or
 680 possess an extended axon.

681 Let n_e represent the number of excitatory cells and n_i represent the number of
 682 inhibitory cells from the set of all cells in the all-all connectome. Define $|k|$ be the
 683 number of potential middle partners. For inhibitory chains, $|k| = n_e$ as the middle cell
 684 is inhibitory. For excitatory chains, the middle cell cannot be the first or final cell, so
 685 $|k| = n_e - 2$.

686 The probability of disynaptic outbound connection for a pre-cell j was calculated
 687 as the proportion of realized disynaptic connections under a given connection type $C \in$
 688 $\{\text{Shared}, \text{Disjoint}\}$, normalized by the total number of potential chains satisfying the
 689 connection type,

$$b_{\text{out}_{j,C}} = \frac{\sum_k \sum_{i|C_{ij}=1} b_{ikj}}{|k| |\{i \mid C_{ij} = 1, i \neq j\}|}.$$

690 Similarly, the probability of disynaptic inbound connection for a post-cell i was
 691 defined as

$$b_{\text{in}_{i,C}} = \frac{\sum_k \sum_{j|C_{ij}=1} b_{ikj}}{|k| |\{j \mid C_{ij} = 1, j \neq i\}|}.$$

692 For nonzero strength of connection, we computed the average realized summed disy-
 693 naptic outbound PSD for a pre-cell j as the total PSD across all chains satisfying the
 694 connection type C , normalized by the number of realized ($b_{ikj} = 1$) chains under C ,

$$w_{\text{out}_{j,C}} = \frac{\sum_k \sum_{i|C_{ij}=1} w_{ikj}}{\sum_k \sum_{i|C_{ij}=1} b_{ikj}}.$$

695 Similarly, the average realized summed disynaptic inbound PSD for a post-cell i was
 696 given by

$$w_{\text{in}_i, \text{C}} = \frac{\sum_k \sum_{j|C_{ij}=1} w_{ikj}}{\sum_k \sum_{j|C_{ij}=1} b_{ikj}}.$$

697 To facilitate statistical testing, we defined collections of metrics based on connection
 698 type C for both monosynaptic and disynaptic analyses. For disynaptic sets, the indices
 699 ij are replaced with ijk appropriately.

700 5.11.3 Set Definitions

701 The following sets were defined to evaluate connectivity metrics:

- 702 • The set of nonzero pairwise connection strengths under a given connection type
 703 C,

$$\{w_{ij} \mid C_{ij} = 1\}.$$

- 704 • The set of outbound probabilities of connection for each pre-cell under a given
 705 connection type C,

$$\{b_{\text{out}_j, \text{C}}\}.$$

706 Similar collections were defined for inbound probability of connection, and for
 707 inbound and outbound nonzero average connection strengths by replacing the
 708 metric accordingly.

- 709 • For inbound or outbound metrics, paired sets were constructed by including only
 710 post- or pre-cells with at least one fulfilled connection under both the Shared and
 711 Disjoint connection types. Let

$$\mathcal{I}_{j,C} = \{i \mid b_{ij} = 1 \text{ and } C_{ij} = 1\}$$

712 be the set of post-cells connected to pre-cell j under connection type C . The set
 713 of pre-cells included in the paired comparison was then defined as:

$$\mathcal{J}_{\text{paired}} = \{j \mid \mathcal{I}_{j,\text{Shared}} \neq \emptyset \wedge \mathcal{I}_{j,\text{Disjoint}} \neq \emptyset\}$$

714 and the paired set of outbound metrics was:

$$\{(b_{\text{out}_j, \text{Shared}}, b_{\text{out}_j, \text{Disjoint}}) \mid j \in \mathcal{J}_{\text{paired}}\}$$

715 Similar paired collections were constructed for inbound probabilities and both
 716 inbound and outbound nonzero average connection strengths, as well as for met-
 717 rics where pre- or post-cells appear in both the Assembly and the Non-Assembly
 718 groups.

719 These sets provided the basis for the statistical tests used to compare metrics across
 720 connection types.

721 5.11.4 Statistical Tests

722 We performed one-way statistical tests at $\alpha = 0.05$ to compare the Shared and
 723 Disjoint groups, as well as to compare the Assembly and Non-Assembly groups. All
 724 alternative hypotheses predict Shared > Disjoint or Assembly > Non-Assembly, except
 725 for tests involving di-synaptic Inhibitory chain sets, in which the alternative hypotheses
 726 predict Shared < Disjoint or Assembly < Non-Assembly. We ran the following tests:

- 727 • For unpaired sets, we use a one-sided Wilcoxon Rank-Sum test
 728 • For paired sets, we use a one-sided paired Wilcoxon Signed-Rank test to compare
 729 metrics within cells appearing in both groups.

730 For pairwise binary connectivity, we created a contingency table to compare the
 731 frequencies of successful and failed connections across connection types:

Connection Type	Successful Connections ($b_{ij} = 1$)	Failed Connections ($b_{ij} = 0$)
Shared	$\sum_{ij Shared_{ij}=1} b_{ij}$	$\sum_{ij Shared_{ij}=1} (1 - b_{ij})$
Disjoint	$\sum_{ij Disjoint_{ij}=1} b_{ij}$	$\sum_{ij Disjoint_{ij}=1} (1 - b_{ij})$

732 Then, we performed a Chi-Squared Test of Independence at $\alpha = 0.05$ to determine
 733 if pairwise connection frequency differs across connection types.

734 Finally, to examine the functional correlates of the di-synaptic inhibitory chain
 735 findings, we calculated the Pearson's correlation coefficient between the summed feed-
 736 forward inhibitory weights of disjoint cells connecting an assembly pair (see Methods
 737 5.11.2) and the correlation scores between the assembly pair's coactivity traces (see
 738 Methods 5.8), and examined significance.

739 **5.11.5 Tail Analysis**

740 In addition to the mono-synaptic and di-synaptic analyses, we performed a “tail”
 741 analysis to investigate whether the proportion of Shared versus Disjoint connections
 742 differs between all pairwise connections and those classified as “tail” connections.

743 To identify “tail” connections, we modeled the distribution of connection strengths
 744 using a Gaussian Mixture Model (GMM) with $k = 2$ components. The model was ini-
 745 tialized via k-means clustering to estimate the weights, means, and standard deviations
 746 of each component. The decision boundary separating the two Gaussian components
 747 was calculated as the intersection of their weighted probability density functions, derived
 748 using a quadratic equation based on the GMM parameters. Connections with values
 749 greater than or equal to the decision boundary were classified as “tail” connections. We
 750 present the model fit and evaluation as well as the tail boundary in the supplemental
 751 figures section (see Supp. Fig. 8).

752 Once the tail connections were identified, we compared the proportions of Shared
 753 and Disjoint connections in this subset to their proportions in the full dataset using a
 754 Chi-Squared Goodness-of-Fit Test at $\alpha = 0.05$. This test considered only the Shared
 755 and Disjoint groups, with expected proportions calculated relative to the total counts
 756 of these two groups in the full dataset.

757 **5.11.6 Centrality analysis**

758 Centrality analysis was used to quantify whether in a given network, assembly cells
 759 were more likely to be central to the network than non-assembly cells. This analysis
 760 gave further insights into the role of assembly cells in higher-order connectivity. To
 761 do this, we measured different centrality metrics for assembly and non-assembly cells,
 762 namely, in-degree centrality, outdegree centrality, closeness centrality, and betweenness
 763 centrality.

764 In a graph, the centrality of a node refers to its tendency to connect and generally
 765 influence other nodes within the network [77]. We developed a directed graph $G =$
 766 (N, E) , using the binary connectome such that $|N|$ represents the number of cells in the
 767 connectome and E represents the binary, directed connections between all cell pairs. The
 768 total number of outbound synaptic connections are given by $\sum_n \deg^+(n)$ and inbound

769 synaptic connections are given by $\sum_n \deg^-(n)$. Normalizing these connections, in-degree
770 centrality was calculated as

$$I = \frac{\sum_n \deg^-(n)}{|N| - 1}$$

771 and outdegree centrality was calculated as

$$D = \frac{\sum_n \deg^+(n)}{|N| - 1}$$

772 where $n \in N$.

773 A monosynaptic connection, $e = (j, i) \in E$ between a pre-cell j and post-cell i , will
774 have i as the head and j as the tail end of the connection, where j and $i \in N$. The
775 path between a pre-cell j acting as a source neuron and a post-cell i acting as a target
776 neuron, is the alternating sequence of cells and connections starting from j and ending
777 at i , with each cell before a connection in the sequence being a pre-cell and each cell
778 after a connection being a post-cell. The number of monosynaptic connections within
779 the path indicates the length of the path. The shortest path between cells j and i is the
780 minimum length between the two cells. The shortest path, ξ_{ij} , is also referred to as the
781 geodesic path.

782 Based on this, the closeness centrality for a given cell i was calculated as the reciprocal
783 of the sum of the shortest paths, or distances between the post-cell i and all other pre-
784 cells j in the graph,

$$V(i) = \frac{|N| - 1}{\sum_{j=1}^N \xi_{ij}}.$$

785 For a given cell k , the betweenness centrality [78] was calculated as

$$B(k) = \sum_{(i,j)} \frac{\xi(k)_{ij}}{\xi_{ij}}$$

786 where $\xi(k)_{ij}$ is the number of shortest paths between pre-cell j and post-cell i that
787 pass through cell k . This value was also normalized to fall between 0 and 1.

788 6 Code Availability

789 All code is available at this GitHub link: <https://github.com/AllenInstitute/HebbsVision>

790 It should be noted that, for all code of our own generation, a fixed random seed
791 is used for reproducibility. Libraries used for analysis and plotting of results include:
792 numpy [79], pandas [80], scikit-learn [81], upsetplot [34], networkx [82], dotmotif [83],
793 matplotlib [84], seaborn [85], and Raincloud [86].

795 7 Acknowledgements

796 We wish to thank the Allen Institute for Brain Science founder, Paul G. Allen, for
797 his vision, encouragement, and support. S.B. has been supported by NIH R01EB029813.
798 S.M. has been in part supported by NSF 2223725, NIH R01EB029813, and RF1DA055669
799 grants.

800 8 List of Contributions

Name	Contributions
J Wagner-Carena	Conception and Design, Functional and Structural Data Analysis, Data Interpretation, Writing, Revision
S Kate	Data Interpretation, Chain and Graph Theoretic Data Analysis, Writing, Revision
T Riordan	Data Interpretation, Statistical Data Analysis, Writing, Revision
R Abbasi-Asl	Data processing, Revision, Writing
J Aman	Coregistration (Data Analysis), Writing
A Amster	Functional ROI extraction, team PIKA
AL Bodor	Data Acquisition: EM Histology/Sectioning; Revision
D Brittain	Data Acquisition: EM Imaging; Revision
JA Buchanan	Data Acquisition: EM Histology; Revision
MA Buice	Data processing: ROI extraction; Revision
DJ Bumbarger	Data Acquisition: EM Sectioning; Revision
F Collman	Interpretation, Dataset Resources and Infrastructure; Revision
NM da Costa	Data Processing; Interpretation; Writing, Revision
DJ Denman	Data Acquisition: Imaging, stimuli
SEJ deVries	Scientific leadership, optical physiology
E Joyce	Data Processing: Skeleton generation, layer definition, soma&nucleus feature extraction; Revision
D Kapner	Data Processing: EM alignment; Revision
CW King	Software development: allen_v1dd library
JD Larkin	Data Acquisition: Functional Imaging
D Liu	Software development: allen_v1dd library
G Mahalingam	Data Processing: EM Image Processing; Revision
D Millman	Stimulus Creation, Data Analysis
J Möller	SGC Algorithm, Writing, Revision
C Morrison	Functional ROI extraction, team PIKA
RC Reid	Interpretation; Dataset Resources and Infrastructure, Revision
CM Schneider-Mizell	Interpretation; Dataset Resources and Infrastructure, Revision
D Scott	Functional ROI extraction, team PIKA
S Suckow	Project Management
KT Takasaki	Data Acquisition: Functional Imaging
M Takeno	Data Acquisition: EM Histology/Sectioning; Data Processing: coRegistration; Revision
R Torres	Data Processing: EM Image Processing/Coregistration; Revision; Writing
D Vumbaco	Proofreading Project Management
J Waters	Microscopy team lead
DG Wyrick	Software development: allen_v1dd library
W Yin	Data Acquisition: EM Imaging; Revision
J Zhuang	Data processing
S Mihalas	Conception and Design, Data Interpretation, Writing, Revision
S Berteau	Conception and Design, Data Analysis, Data Interpretation, Writing, Revision

801 References

- 802 [1] Hebb, D. *The Organization of Behavior* (John Wiley & Sons, New York, 1949).
- 803 [2] Frégnac, Y. Aplysia: Hebbian or not? *Trends in Neurosciences* **9**, 410 (1986).
- 804 [3] Buzsáki, G. Neural Syntax: Cell Assemblies, Synapsembles, and Readers. *Neuron* **68**, 362–385 (2010).
- 805 [4] Miehl, C., Onasch, S., Festa, D. & Gjorgjieva, J. Formation and computational
806 implications of assemblies in neural circuits. *The Journal of Physiology* **601**, 3071–
807 3090 (2023).
- 808 [5] Matheus Gauy, M. *et al.* A Hippocampal Model for Behavioral Time Acquisition
809 and Fast Bidirectional Replay of Spatio-Temporal Memory Sequences. *Frontiers in*
810 *Neuroscience* **12**, 961 (2018).
- 811 [6] Carrillo-Reid, L., Miller, J.-E. K., Hamm, J. P., Jackson, J. & Yuste, R. Endogenous
812 sequential cortical activity evoked by visual stimuli. *The Journal of Neuroscience: The Official Journal of the Society for Neuroscience* **35**, 8813–8828 (2015).
- 813 [7] MacLean, J. N., Watson, B. O., Aaron, G. B. & Yuste, R. Internal Dynamics
814 Determine the Cortical Response to Thalamic Stimulation. *Neuron* **48**, 811–823
815 (2005).
- 816 [8] Pérez-Ortega, J., Alejandre-García, T. & Yuste, R. Long-term stability of cortical
817 ensembles. *eLife* **10**, e64449 (2021). Publisher: eLife Sciences Publications, Ltd.
- 818 [9] Hebb, D. O. The semiautonomous process: Its nature and nurture. *American
819 Psychologist* **18**, 16–27 (1963). Place: US Publisher: American Psychological Association.
- 820 [10] Brock, L. G., Coombs, J. S. & Eccles, J. C. The recording of potentials from
821 motoneurones with an intracellular electrode. *The Journal of Physiology* **117**, 431–
822 460 (1952).
- 823 [11] Marr, D. & Brindley, G. S. Simple memory: a theory for archicortex. *Philosophical
824 Transactions of the Royal Society of London. B, Biological Sciences* **262**, 23–81
825 (1997). Publisher: Royal Society.
- 826 [12] Traub, R. D., Tu, Y. & Whittington, M. A. Cell assembly formation and structure
827 in a piriform cortex model. *Reviews in the Neurosciences* **33**, 111–132 (2022).
- 828 [13] Gastaldi, C., Schwalger, T., Falco, E. D., Quiroga, R. Q. & Gerstner, W. When
829 shared concept cells support associations: Theory of overlapping memory engrams.
830 *PLOS Computational Biology* **17**, e1009691 (2021). Publisher: Public Library of
831 Science.
- 832 [14] Holtmaat, A. & Caroni, P. Functional and structural underpinnings of neuronal
833 assembly formation in learning. *Nature Neuroscience* **19**, 1553–1562 (2016).
- 834 [15] Grinvald, A., Arieli, A., Tsodyks, M. & Kenet, T. Neuronal assemblies: Single
835 cortical neurons are obedient members of a huge orchestra. *Biopolymers* **68**, 422–
836 436 (2003).
- 837 [16] Harris, K. D. Neural signatures of cell assembly organization. *Nature Reviews
838 Neuroscience* **6**, 399–407 (2005). Number: 5 Publisher: Nature Publishing Group.
- 839

- 842 [17] Harris, K. D., Csicsvari, J., Hirase, H., Dragoi, G. & Buzsáki, G. Organization of
843 cell assemblies in the hippocampus. *Nature* **424**, 552–556 (2003).
- 844 [18] Kamiński, J. *et al.* Persistently active neurons in human medial frontal and medial
845 temporal lobe support working memory. *Nature Neuroscience* **20**, 590–601 (2017).
- 846 [19] Wilson, M. A. & McNaughton, B. L. Reactivation of hippocampal ensemble mem-
847 ories during sleep. *Science (New York, N.Y.)* **265**, 676–679 (1994).
- 848 [20] Yuste, R., Nelson, D. A., Rubin, W. W. & Katz, L. C. Neuronal domains in
849 developing neocortex: mechanisms of coactivation. *Neuron* **14**, 7–17 (1995).
- 850 [21] Sherafati, A. *et al.* Depth-dependant heterogeneity of neuronal responses in mouse
851 primary visual cortex}. *BioRxiv* (2025).
- 852 [22] Grienberger, C. & Konnerth, A. Imaging Calcium in Neurons. *Neuron* **73**, 862–885
853 (2012). Publisher: Elsevier.
- 854 [23] Scheffer, L. K. *et al.* A connectome and analysis of the adult Drosophila central
855 brain. *eLife* **9**, e57443 (2020). Publisher: eLife Sciences Publications, Ltd.
- 856 [24] Dorkenwald, S. *et al.* Neuronal wiring diagram of an adult brain. *Nature* **634**,
857 124–138 (2024). Publisher: Nature Publishing Group.
- 858 [25] Witvliet, D. *et al.* Connectomes across development reveal principles of brain mat-
859 uration. *Nature* **596**, 257–261 (2021). Number: 7871 Publisher: Nature Publishing
860 Group.
- 861 [26] Gour, A. *et al.* Postnatal connectomic development of inhibition in mouse barrel
862 cortex. *Science (New York, N.Y.)* **371**, eabb4534 (2021).
- 863 [27] Bae, J. A. *et al.* Functional connectomics spanning multiple areas of mouse visual
864 cortex. *Nature* **640**, 435–447 (2025). Publisher: Nature Publishing Group.
- 865 [28] Shapson-Coe, A. *et al.* A petavoxel fragment of human cerebral cortex reconstructed
866 at nanoscale resolution. *Science* **384**, eadk4858 (2024). Publisher: American Asso-
867 ciation for the Advancement of Science.
- 868 [29] Bock, D. D. *et al.* Network anatomy and in vivo physiology of visual cortical
869 neurons. *Nature* **471**, 177–182 (2011).
- 870 [30] Lee, W.-C. A. *et al.* Anatomy and function of an excitatory network in the visual
871 cortex. *Nature* **532**, 370–374 (2016). Number: 7599 Publisher: Nature Publishing
872 Group.
- 873 [31] Massey, F. J. The Kolmogorov-Smirnov Test for Goodness of Fit. *Journal of the*
874 *American Statistical Association* **46**, 68–78 (1951). Publisher: [American Statistical
875 Association, Taylor & Francis, Ltd.].
- 876 [32] Tootell, R. B. H. *et al.* Functional analysis of primary visual cortex (V1) in humans.
877 *Proceedings of the National Academy of Sciences* **95**, 811–817 (1998). Publisher:
878 Proceedings of the National Academy of Sciences.
- 879 [33] Möller, J., Avitan, L. & Goodhill, G. J. Detecting neural assemblies in calcium
880 imaging data. *BMC biology* **16**, 143 (2018).

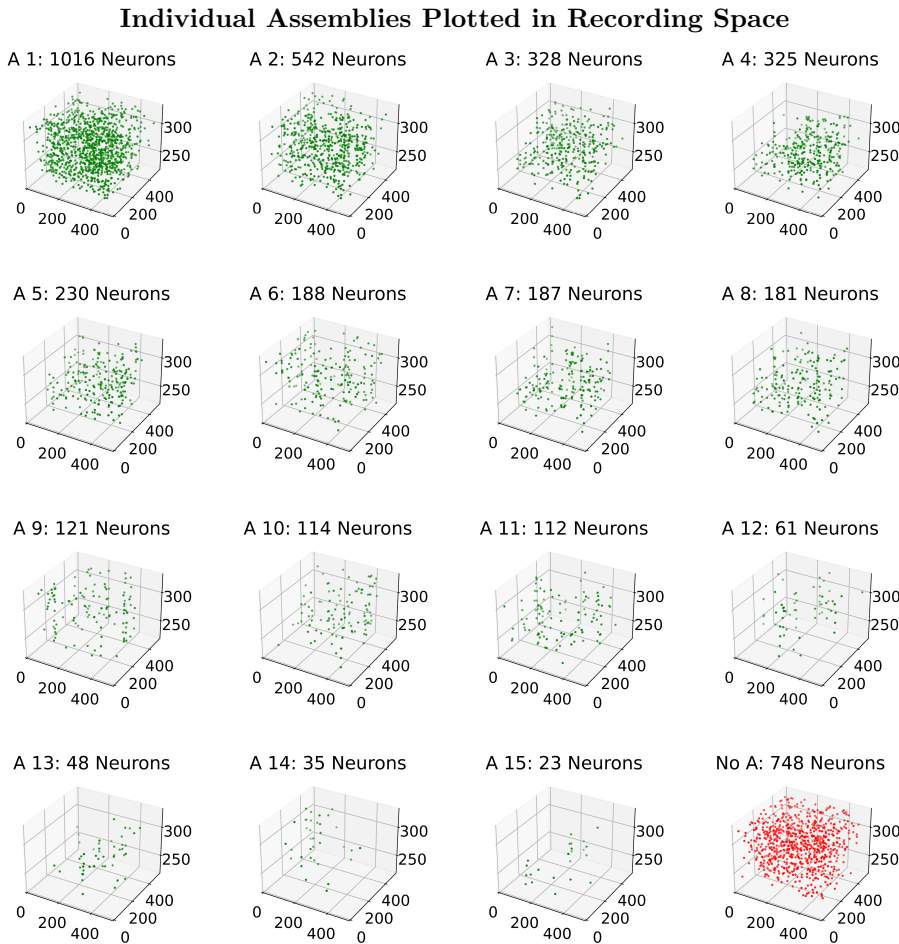
- 881 [34] Lex, A., Gehlenborg, N., Strobelt, H., Vuillemot, R. & Pfister, H. UpSet: Visu-
882 alization of Intersecting Sets. *IEEE Transactions on Visualization and Computer*
883 *Graphics* **20**, 1983–1992 (2014). Conference Name: IEEE Transactions on Visual-
884 ization and Computer Graphics.
- 885 [35] Dorfman, R. A Formula for the Gini Coefficient. *The Review of Economics and*
886 *Statistics* **61**, 146–149 (1979). Publisher: The MIT Press.
- 887 [36] Walker, E. Y. *et al.* Inception loops discover what excites neurons most using
888 deep predictive models. *Nature Neuroscience* **22**, 2060–2065 (2019). Number: 12
889 Publisher: Nature Publishing Group.
- 890 [37] Green, M. Contrast detection and direction discrimination of drifting gratings.
891 *Vision Research* **23**, 281–289 (1983).
- 892 [38] Abdel-aziem, A. H. & Soliman, T. H. M. A Multi-Layer Perceptron (MLP) Neu-
893 ral Networks for Stellar Classification: A Review of Methods and Results. *Inter-
894 national Journal of Advances in Applied Computational Intelligence* **Volume 3**,
895 29–37 (2023). Publisher: American Scientific Publishing Group (ASPG).
- 896 [39] Bhatkar, A. P. & Kharat, G. Detection of Diabetic Retinopathy in Retinal Images
897 Using MLP Classifier. In *2015 IEEE International Symposium on Nanoelectronic*
898 *and Information Systems*, 331–335 (2015).
- 899 [40] Alon, U. Network motifs: theory and experimental approaches. *Nature Reviews*
900 *Genetics* **8**, 450–461 (2007). Number: 6 Publisher: Nature Publishing Group.
- 901 [41] Sporns, O. & Kötter, R. Motifs in Brain Networks. *PLoS Biology* **2**, e369 (2004).
- 902 [42] Hu, Y., Trousdale, J., Josić, K. & Shea-Brown, E. Motif statistics and spike corre-
903 lations in neuronal networks. *Journal of Statistical Mechanics: Theory and Experi-
904 ment* **2013**, P03012 (2013). Publisher: IOP Publishing and SISSA.
- 905 [43] Hebb, D. O. Intelligence, Brain Function and The Theory of Mind. *Brain* **82**,
906 260–275 (1959).
- 907 [44] Holtmaat, A. & Svoboda, K. Experience-dependent structural synaptic plasticity in
908 the mammalian brain. *Nature Reviews Neuroscience* **10**, 647–658 (2009). Number:
909 9 Publisher: Nature Publishing Group.
- 910 [45] Mongillo, G., Rumpel, S. & Loewenstein, Y. Intrinsic volatility of synaptic connec-
911 tions — a challenge to the synaptic trace theory of memory. *Current Opinion in*
912 *Neurobiology* **46**, 7–13 (2017).
- 913 [46] Aitken, K., Garrett, M., Olsen, S. & Mihalas, S. The geometry of representational
914 drift in natural and artificial neural networks. *PLOS Computational Biology* **18**,
915 e1010716 (2022). Publisher: Public Library of Science.
- 916 [47] Schoonover, C. E., Ohashi, S. N., Axel, R. & Fink, A. J. P. Representational drift
917 in primary olfactory cortex. *Nature* **594**, 541–546 (2021). Number: 7864 Publisher:
918 Nature Publishing Group.
- 919 [48] Olshausen, B. A. & Field, D. J. Sparse coding of sensory inputs. *Current Opinion*
920 *in Neurobiology* **14**, 481–487 (2004).
- 921 [49] Okun, M. *et al.* Diverse coupling of neurons to populations in sensory cortex.
922 *Nature* **521**, 511–515 (2015). Publisher: Nature Publishing Group.

- 923 [50] Yuste, R., Cossart, R. & Yaksi, E. Neuronal ensembles: Building blocks of neural
924 circuits. *Neuron* S0896-6273(23)00967-4 (2024).
- 925 [51] Vogels, T. P. & Abbott, L. F. Gating multiple signals through detailed balance
926 of excitation and inhibition in spiking networks. *Nature Neuroscience* **12**, 483–491
927 (2009). Publisher: Nature Publishing Group.
- 928 [52] Vogels, T. P., Sprakler, H., Zenke, F., Clopath, C. & Gerstner, W. Inhibitory
929 Plasticity Balances Excitation and Inhibition in Sensory Pathways and Memory
930 Networks. *Science* **334**, 1569–1573 (2011). Publisher: American Association for
931 the Advancement of Science.
- 932 [53] Xu, S. *et al.* Behavioral state coding by molecularly defined paraventricular hy-
933 pothalamic cell type ensembles. *Science* **370**, eabb2494 (2020). Publisher: Ameri-
934 can Association for the Advancement of Science.
- 935 [54] de Vries, S. E. J. *et al.* A large-scale standardized physiological survey reveals
936 functional organization of the mouse visual cortex. *Nature Neuroscience* **23**, 138–
937 151 (2020). Publisher: Nature Publishing Group.
- 938 [55] Hua, Y., Laserstein, P. & Helmstaedter, M. Large-volume en-bloc staining for
939 electron microscopy-based connectomics. *Nature Communications* **6**, 7923 (2015).
940 Publisher: Nature Publishing Group.
- 941 [56] Yin, W. *et al.* A petascale automated imaging pipeline for mapping neuronal circuits
942 with high-throughput transmission electron microscopy. *Nature Communications*
943 **11**, 4949 (2020). Publisher: Nature Publishing Group.
- 944 [57] Macrina, T. *et al.* Petascale neural circuit reconstruction: automated methods
945 (2021). Pages: 2021.08.04.455162 Section: New Results.
- 946 [58] Phelps, J. S. *et al.* Reconstruction of motor control circuits in adult Drosophila
947 using automated transmission electron microscopy. *Cell* **184**, 759–774.e18 (2021).
948 Publisher: Elsevier.
- 949 [59] Mahalingam, G. *et al.* A scalable and modular automated pipeline for stitching
950 of large electron microscopy datasets. *eLife* **11**, e76534 (2022). Publisher: eLife
951 Sciences Publications, Ltd.
- 952 [60] Schneider-Mizell, C. M. *et al.* Inhibitory specificity from a connectomic census of
953 mouse visual cortex. *Nature* **640**, 448–458 (2025). Publisher: Nature Publishing
954 Group.
- 955 [61] Dorkenwald, S. *et al.* CAVE: Connectome Annotation Versioning Engine (2023).
956 Pages: 2023.07.26.550598 Section: New Results.
- 957 [62] Schindelin, J. *et al.* Fiji: an open-source platform for biological-image analysis.
958 *Nature Methods* **9**, 676–682 (2012). Publisher: Nature Publishing Group.
- 959 [63] Bogovic, J. A., Hanslovsky, P., Wong, A. & Saalfeld, S. Robust registration of
960 calcium images by learned contrast synthesis. In *2016 IEEE 13th International
961 Symposium on Biomedical Imaging (ISBI)*, 1123–1126 (2016). ISSN: 1945-8452.
- 962 [64] Avitan, L. *et al.* Spontaneous Activity in the Zebrafish Tectum Reorganizes over
963 Development and Is Influenced by Visual Experience. *Current Biology* **27**, 2407–
964 2419.e4 (2017). Publisher: Elsevier.

- 965 [65] Almeida-Filho, D. G. *et al.* An investigation of Hebbian phase sequences as assembly
966 graphs. *Frontiers in Neural Circuits* **8**, 34 (2014).
- 967 [66] Kursin, A., Húsek, D. & Neruda, R. Faster Learning with Overlapping Neural
968 Assemblies. In Kollias, S. D., Stafylopatis, A., Duch, W. & Oja, E. (eds.) *Artificial
969 Neural Networks – ICANN 2006*, Lecture Notes in Computer Science, 226–233
970 (Springer, Berlin, Heidelberg, 2006).
- 971 [67] Möller, J. & Goodhill, G. J. Detecting Neural Assemblies Through Similarity
972 Graph Clustering. In Carrillo-Reid, L. (ed.) *Identification, Characterization, and
973 Manipulation of Neuronal Ensembles*, 167–176 (Springer US, New York, NY, 2025).
- 974 [68] Miller, R. G. A Trustworthy Jackknife. *The Annals of Mathematical Statistics* **35**,
975 1594–1605 (1964). Publisher: Institute of Mathematical Statistics.
- 976 [69] Richter, C. G., Thompson, W. H., Bosman, C. A. & Fries, P. A jackknife approach
977 to quantifying single-trial correlation between covariance-based metrics undefined
978 on a single-trial basis. *NeuroImage* **114**, 57–70 (2015).
- 979 [70] Hurley, N. & Rickard, S. Comparing Measures of Sparsity. *IEEE Transactions on
980 Information Theory* **55**, 4723–4741 (2009). Conference Name: IEEE Transactions
981 on Information Theory.
- 982 [71] Khosravy, M., Nitta, N., Gupta, N., Patel, N. & Babaguchi, N. Chapter 3 - A
983 descriptive review to sparsity measures. In Khosravy, M., Dey, N. & Duque, C. A.
984 (eds.) *Compressive Sensing in Healthcare*, Advances in ubiquitous sensing applica-
985 tions for healthcare, 43–63 (Academic Press, 2020).
- 986 [72] Wright Muelas, M., Mughal, F., O'Hagan, S., Day, P. J. & Kell, D. B. The role
987 and robustness of the Gini coefficient as an unbiased tool for the selection of Gini
988 genes for normalising expression profiling data. *Scientific Reports* **9**, 17960 (2019).
989 Number: 1 Publisher: Nature Publishing Group.
- 990 [73] Hetherington, P. A., & Shapiro, M. L. Simulating Hebb cell assemblies: the neces-
991 sity for partitioned dendritic trees and a post-not-pre LTD rule. *Network: Compu-
992 tation in Neural Systems* **4**, 135–153 (1993). Publisher: Taylor & Francis.
- 993 [74] Garagnani, M., Wennekers, T. & Pulvermüller, F. Recruitment and Consolidation
994 of Cell Assemblies for Words by Way of Hebbian Learning and Competition in a
995 Multi-Layer Neural Network. *Cognitive Computation* **1**, 160–176 (2009).
- 996 [75] Fransen, E., Lansner, A. & Liljenström, H. A Model of Cortical Associative Memory
997 Based on Hebbian Cell Assemblies. In Eeckman, F. H. & Bower, J. M. (eds.)
998 *Computation and Neural Systems*, 431–435 (Springer US, Boston, MA, 1993).
- 999 [76] Dorkenwald, S. *et al.* Binary and analog variation of synapses between cortical
1000 pyramidal neurons. *eLife* **11**, e76120 (2022). Publisher: eLife Sciences Publications,
1001 Ltd.
- 1002 [77] Bavelas, A. A Mathematical Model for Group Structures. *Human Organization* **7**,
1003 16–30 (2009).
- 1004 [78] Freeman, L. C. A Set of Measures of Centrality Based on Betweenness. *Sociometry*
1005 **40**, 35–41 (1977). Publisher: [American Sociological Association, Sage Publications,
1006 Inc.].
- 1007 [79] Harris, C. R. *et al.* Array programming with NumPy. *Nature* **585**, 357–362 (2020).
1008 Publisher: Nature Publishing Group.

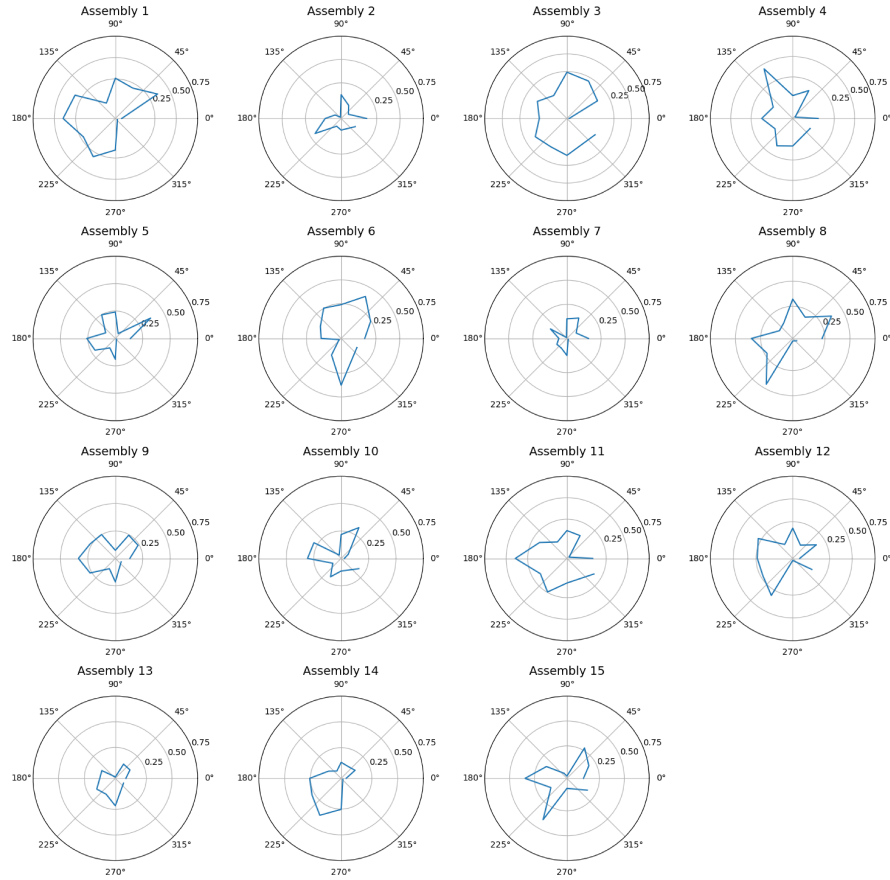
- 1009 [80] McKinney, W. Data Structures for Statistical Computing in Python. *scipy* (2010).
- 1010 [81] Pedregosa, F. *et al.* Scikit-learn: Machine Learning in Python. *Journal of Machine*
1011 *Learning Research* **12**, 2825–2830 (2011).
- 1012 [82] Hagberg, A. A., Schult, D. A. & Swart, P. J. Exploring Network Structure, Dy-
1013 namics, and Function using NetworkX. *scipy* (2008).
- 1014 [83] Matelsky, J. K. *et al.* DotMotif: an open-source tool for connectome subgraph
1015 isomorphism search and graph queries. *Scientific Reports* **11**, 13045 (2021).
- 1016 [84] Hunter, J. D. Matplotlib: A 2D Graphics Environment. *Computing in Science &*
1017 *Engineering* **9**, 90–95 (2007). Conference Name: Computing in Science & Engi-
1018 neering.
- 1019 [85] Waskom, M. L. seaborn: statistical data visualization. *Journal of Open Source*
1020 *Software* **6**, 3021 (2021).
- 1021 [86] Micah, A. *et al.* Raincloud plots: a multi-platform tool for robust data visualization.
1022 *Wellcome Open Research* (2021).

1023 **9 Supplemental Figures**



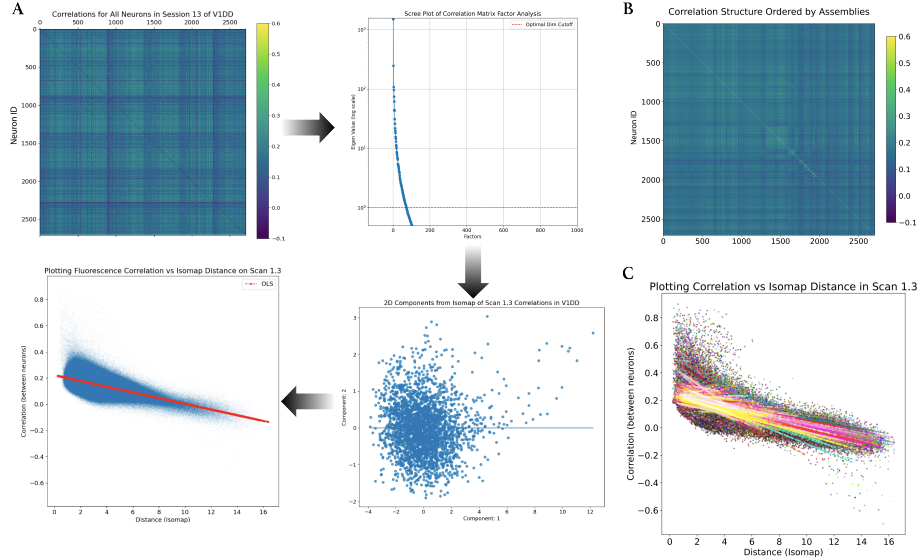
Supplementary Figure 1. Spatial positions of individual extracted assemblies in the three-dimensional recording field. Every subplot provides an isolated view of an assembly, ordered by size, visualized in the optical imaging recording space. Each individual point refers to an identified excitatory neuron. The plot of neurons assigned to no assemblies, ‘No A’, is also shown in red (bottom-right). Sub-plot axes refer to the three spatial dimensions of the recording field, with units in micrometers. Sub-plot titles also include the size of each assembly. In total, 1960 neurons were assigned to assemblies, and 748 were not. Assemblies are typically spatially spread out throughout the recording field.

Assembly Oracle Scores as a function of Fullscreen Grating Orientations

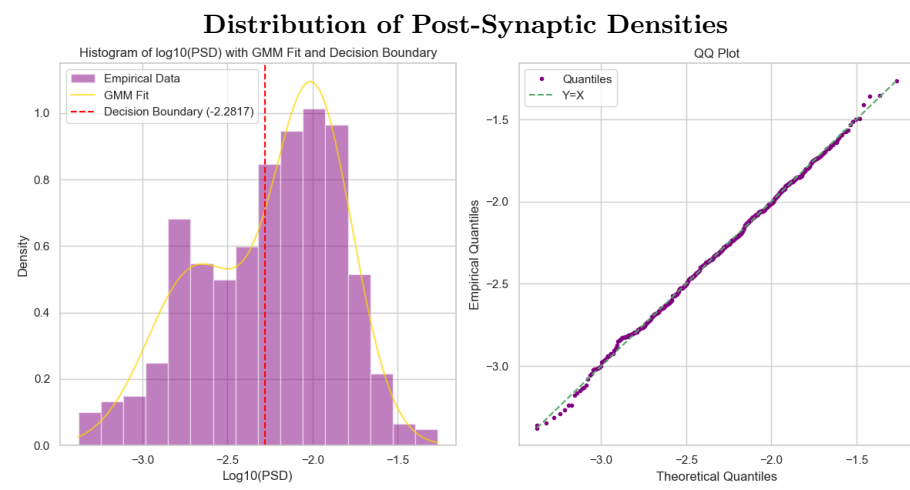


Supplementary Figure 2. Individual Assemblies Oracle Scores to Fullscreen Gratings. Every sub-plot provides an isolated visualization of the reliability in an assembly's response with respect to the orientation of fullscreen gratings. Orientation of gratings is represented by a polar plot. Reliability is measured through the Oracle score metric (see Methods 5.3). The scores of assembly coactivity trace in response to gratings are typically lower than those seen in natural movies (Fig. 3C), but the results are still indicative of tuning properties in these functional populations. Notably, some assembly traces seem to be highly reliable to particular orientations, similar to the orientation receptive fields of simple cells in the primary visual cortex.

Low-Dimensional Description of Pairwise Activity Correlations



Supplementary Figure 3. Fitting Regressions to establish low-dimensional descriptions of pairwise activity correlations of cells. This framework was used to choose the optimal hyperparameters from Scan Volume 4, with those parameters later being chosen for Scan Volume 3. **(A)**. Pipeline to produce our regression fits to activity correlations. *Top-left*: The procedure begins with the pairwise correlation matrix of the whole scan throughout the hour recording. *Top-right*: Factor analysis reveals which dimensions of the original data matrix explain the most variance. This is done by plotting the eigenvalue of each factor, or dimension. The dotted red line is a horizontal marker of the eigenvalue of one, a threshold for considered dimensions justified by the Kaiser criterion. We ensure that at least ninety percent of the total variance is left explained in the final embedding. Less than fifty factors, or dimensions, are needed to do so. *Bottom-right*: With these dimensions in mind, we apply Isomap to produce a non-linear low-dimensional manifold of the original correlation matrix. This plot illustrates the first and second components from that embedding. *Bottom-right*: Finally, our low-dimensional description of the activity correlation, or our activity correlation space, is produced by plotting the distance of neurons across the Isomap embedding with respect to their pairwise correlations. The OLS fit (solid-red line) is a statistical model exemplifying how well the system continuum is able to describe this activity correlation space. **(B)** Correlation matrix of the whole scan with neurons ordered by assemblies. Cells on each axis were ordered by their largest corresponding assembly, from ‘A 1’ to ‘A 15’. **(C)** OLS fits were developed that corresponded to assembly assignments with pairwise cells. This implies that multiple OLS fits were performed to account for all assignments. Regression fits to different assembly assignments are compared through the Akaike information criterion.



Supplementary figure 4. Histogram of connection strengths (log10-scaled) with GMM fit overlaid, and QQ plot evaluating the fit. The red dashed line indicates the decision boundary separating the two Gaussian components, used to classify “tail” connections.